Quantitative photoacoustic spectral transformations in theranostic Solid Lipid Nanoparticles labelled with increasing concentrations of a Photoacoustic NIR BODIPY †

Clément Linger,[a,b] Giulia Maccini,[a] Gilles Clavier,[c] Rachel Méallet,[d] Nicolas Tsapis,‡*[a] and Jérôme Gateau ‡*[b]

Solid lipid nanoparticles (SLNs) have shown great capabilities for drug delivery and are therefore attractive theranostic candidates when labelled with an imaging contrast agent. This work aims to create the first SLNs labelled for photoacoustic (PA) imaging by encapsulating a specially designed and near-infrared absorbing BODIPY dye (BY-aniline-Palm) into SLNs of dexamethasone palmitate. A one-pot formulation protocol enabled us to replace the prodrug by the BY-aniline-Palm label in various proportions up to 100%. Increasing the dye content exhibited complex but gradual transformations of the SLNs in terms of optical absorption and PA spectra, and the formation of aggregates at high concentration. A comprehensive and quantitative PA spectrometric study revealed a photoacoustic generation efficiency (PGE) that is spectrally varying and notably greater than 1. A joined spectral decomposition of the absorption and PA spectra into a sum of three Gaussian functions displayed a per-band evolution of the PGE when the concentration of BY-aniline-Palm varied and showed an interplay between the bands with a constant spectrum area. Finally, a novel quantitative PA spectroscopic approach, involving measurements at three different ambient temperatures, demonstrated that the remarkable PGE values arise from a significant thermo-elastic expansion of the SLN during the PA signal generation independently of the absorption band. This study highlights that labeled SLNs are promising agents for PA imaging and also unveils complex transformations that can occur in such nanosystems with a dye prone to aggregation.

A. Introduction

Solid Lipid Nanoparticles (SLNs) are increasingly studied for therapeutic applications because of their ability to deliver mostly hydrophobic drugs[1]. SLNs consist of a matrix of biocompatible solid lipids stabilized by surfactants. They are highly stable thanks to their solid structure, show poor toxicity and are easily scalable at low cost[1]. Lorscheider et al. recently developed a simple one-pot formulation protocol for dexamethasone palmitate (DXP) SLNs[2,3]. DXP is a prodrug of dexamethasone, an anti-inflammatory drug, released by enzymatic cleavage once these SLNs are administered *in vivo*. The anti-inflammatory activity of DXP SLNs was demonstrated *in vivo* in a murine model of rheumatoid arthritis and the nanoparticles exhibited very promising therapeutic effects. SLNs can become theranostic agents with the co-encapsulation of imaging contrast agents, and have already been used for MRI image-guided therapy [4,5]. Investigations for optical imaging are just emerging, with at least one study[6] in which hydrophobic methine dyes were encapsulated in SLNs for fluorescence imaging.

Fluorescence imaging and photoacoustic imaging (PAI) are the main optical bioimaging modalities for applications at centimetre depth[7], when operating in the Near InfraRed (NIR), also called the optical window of biological tissues (typically between 650 and 1300 nm). The high sensibility of these modalities to molecular contrast is a real asset to monitor the accumulation of drug-loaded nanoparticles. PAI is based on the transformation of absorbed optical energy into ultrasound, through photothermal conversion and thermo-elastic expansion[8]. This ultrasound generation and subsequent detection yield to images with a submillimetre spatial resolution, particularly adapted to theranostic applications in focal lesions. Photoacoustic imaging at different successive excitation wavelengths (called multispectral PAI) allows the spectral separation of absorbers[9]. At each wavelength, the amplitude of the emitted ultrasound signal is proportional to the absorbed energy converted into heat, which calls, in terms of optical properties of theranostic SLNs, for a high photothermal conversion efficiency (PTCE) and a large absorption cross section in the NIR range. As for the absorption spectrum, NIR dyes are attractive PAI molecular contrast agents because of the presence of absorption bands providing a spectral signature different from the ones of haemoglobin[9], and thereby facilitating spectral unmixing from the main endogenous absorber.

Among the variety of NIR dyes developed for PAI[10], BODIPYs hold a promising position. Indeed, the BODIPY scaffold is a versatile electron withdrawing platform, and the addition of electron-donating groups allows for the fine tuning of the maximum absorption wavelength in the visible and NIR ranges and favours fluorescence quenching. The high molar extinction coefficients of BODIPY dyes, their strong photostability, and low de-excitation through triplet state transition also favours the development of molecular photoacoustic agents[10]. Several studies reported the use of BODIPY in nanoparticle

[a.] *Université Paris-Saclay, CNRS, Institut Galien Paris-Saclay, 91400 Orsay, France.*

[b.] *Sorbonne Université, CNRS, INSERM, Laboratoire d'Imagerie Biomédicale, 75006 Paris, France.*

[c.] Université Paris-Saclay, ENS Paris-Saclay, CNRS, PPSM, 91190 Gif-sur-Yvette, France.

[d.] *Université Paris-Saclay, CNRS, Institut des Sciences Moléculaires d'Orsay, 91405 Orsay, France.*

* Correspondence: jerome.gateau@sorbonne-universite.fr and nicolas.tsapis@universite-paris-saclay.fr

‡ Equal leading contribution.

† Electronic Supplementary Information (ESI) available

assemblies[11], with possibly high molecular loading to enhance the per-particle absorption, and thus PAI detectability. Unlike widespread heptamethine cyanine dyes[9], such as indocyanine green (ICG) or cyanine-7 (Cy7), BODIPY are not amphiphilic but highly hydrophobic, which proves to be advantageous for their encapsulation into hydrophobic particles. In this context, Bodin *et al.*[12] developed a BODIPY-aniline (BY-aniline) presenting a high molar extinction coefficient at 753 nm ($\sim 8 \times 10^5$ L·mol^{-1}·cm^{-1}) and a superior photostability compare to Cy7. BY-aniline was grafted with a poly(lactic acid) (PLA) chain by ring-opening polymerization and formulated into polymer nanoparticles. The nanoparticles did not show cytotoxicity and, once injected intravenously into mice, provided detectable contrast agent for multispectral PAI.

To label SLNs with a BODIPY dye for PAI-based theranostic applications, we investigate here BY-aniline loading in DXP SLNs. For this purpose, BY-aniline was grafted to a palmitate chain and loaded into DXP SLNs at different BY-aniline-palmitate/DXP ratios. Then, formulated SLNs were thoroughly characterized in terms of optical and photoacoustic (PA) properties. Quantitative PA characterization was performed with a recently developed and novel calibrated photoacoustic spectrometer[13]. The great strength of this PA spectrometer lies in the calibration of the system, which yields quantitative spectral measurements directly comparable to the absorption spectrum, unlike prevalent PA spectra in arbitrary units[14]. The global and per-band quantitative comparison between PA and absorption spectra of BY-aniline loaded PLA particles recently revealed the appearance of non-linearity in the PA spectrum. This non-linearity was caused by a reduction in the photoacoustic efficiency for one absorption band when the laser fluence increases and the dye concentration decreases. The phenomenon was attributed to ground state depopulation of the fluorescent BY-aniline and was reduced by the 'aggregation caused quenching' effect[15]. These novel results in the domain of dye loaded nanoparticles for PAI have encouraged the present study on new particles labelled with BY-aniline, especially with much higher dye loading which would strongly increase the per-particle photoacoustic brightness[15] and could cause further aggregation of the dye.

In this paper, we present the first SLNs tailored for PAI using a NIR BODIPY. The versatility of the formulation enabled us to create SLNs with an extended range of BY-aniline concentrations, reaching very attractive absorption and PA molar coefficients for PAI detectability. Strong spectral modifications were also revealed with the increasing dye concentration, up to the appearance of a new spectral band at high concentration. Moreover, quantitative PA coefficients unveiled a photoacoustic efficiency higher than expected and spectrally varying. These surprising PA features were further characterized with additional PA measurements at different temperatures and a band decomposition of the spectra to investigate their origin.

The formulation of Solid Lipid Nanoparticles (SLN) was adapted from Lorscheider *et al.*[2,3] and relies on an emulsion-evaporation protocol. The PA BODIPY-aniline dye (BY-aniline) synthesized by Bodin *et al.*[12] was esterified on its alcohol function, using a palmitate chain to yield BY-aniline-Palm. Chemical grafting prevents dye leakage from the SLNs and limits burst release.

Dye loading in the SLNs was investigated in a large range by varying the molar ratio of BY-aniline-Palm and DXP, up to completely replacing the prodrug by the dye. A first batch (Batch #1) containing nine molar percentages of BY-aniline-Palm compared to DXP was formulated: SLN-0%, SLN-1%, SLN-2%, SLN-6%, SLN-12%, SLN-25%, SLN-50%, SLN-75% and SLN-100%. All nanoparticles were prepared the very same day. Fig. 1(c) shows the nine suspensions that appear darker as the BY-aniline-Palm percentage increases.

Each formulation was characterized by zeta potential, dynamic light scattering (DLS) and transmission electron microscopy (TEM). Characteristics of SLN-0% (without BY-aniline-Palm) match those reported by Lorscheider *et al.*[2], with an hydrodynamic diameter of 160 nm, a polydispersity index (PdI) of 0.18 and a zeta potential of -58 mV. For all SLNs, the zeta potential was found negative, with values slightly increasing with the BY-aniline-Palm percentage from -58 mV for SLN-0% to -45 mV for SLN-100% (Fig. S7), suggesting a colloidal stability by electrostatic and steric repulsions of all suspensions. The hydrodynamic diameter determined by DLS (Fig. 1(a)) is stable ~170 nm for BY-aniline-Palm percentage up to 50% and then decreases down to 125 nm for SLN-100%. The PdI is below 0.2 for BY-aniline-Palm percentage up to 25% and then increases to reach 0.39 for SLN-100% (Fig. 1(b)). The stability over time was assessed with DLS measurements: all the formulations are stable for at least one month when stored at 4°C and for at least 4 days at 37°C. TEM images in Fig. 1(d) show quite monodisperse spherical particles for SLN-0% and SLN-1% (small dots in the background are likely to be DSPE-PEG$_{2000}$ micelles). However, the appearance and size of individual SLNs becomes increasingly heterogeneous as BY-aniline-Palm percentage increases. The global shape of the particles becomes less spherical and the surface becomes more facetted for BY-aniline-Palm content above 25%, as shown by Fig. 1(d) and Fig. S8. The increase of polydispersity is confirmed by TEM with smaller egg-shaped particles for SLN-100%.
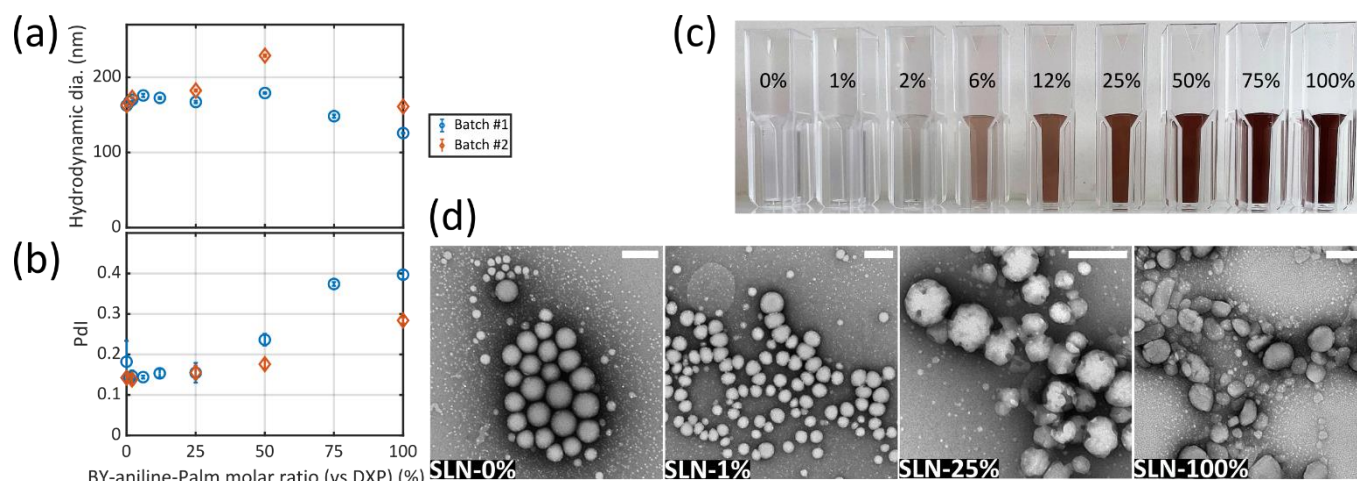
B. Results

B.1. Formulation and colloidal suspension characterisation

Fig. 1 – (a) SLN hydrodynamic diameter measured by dynamic light scattering and (b) SLN polydispersity index (PdI) as a function of the molar ratio of BY-aniline-Palm versus DXP. Mean values and error bars (standard deviation) of triplicate measurements. Markers are blue circles for Batch #1 and orange diamonds for Batch #2. (c) Picture of the BY-aniline-Palm concentration ladder created by the 9 SLN formulations of Batch #1 (percentages referring to the molar proportion of BY-aniline-Palm versus DXP). For the sake of visibility, each sample is a 50-fold dilution of formulation result. (d) SLN TEM images with negative staining (uranyl acetate 2% w/w) obtained with JEOL JEM-1400 microscope at an acceleration voltage of 120 kV. Magnifications for SLN-0%, SLN-1%, SLN-25% and SLN-100% are 15,000, 12,000, 25,000 and 15000, respectively. White scale bars on the top right corner represent 200 nm.

To assess the formulation reproducibility and perform additional characterizations, a second batch (Batch #2) was formulated 8 months later and for the five molar percentages: SLN-0%, SLN-2%, SLN-25%, SLN-50% and SLN-100%. While not exactly identical as Batch #1, SLNs of Batch #2 have globally similar characteristics as for Batch #1, and follow the same trends. Indeed, zeta potential (Fig. S7), hydrodynamic diameter (Fig. 1(a)) and PdI (Fig. 1(b)) showed identical variations as Batch #1 as a function of BY-palm ratio.

Therefore, the developed PA-tailored SLN formulation is reproducible in terms of nanoparticles size, dispersity and surface charge.

B.2. Colloidal suspension comparison with BY-aniline-PLA particles

In a previous study by our consortium[12], BY-aniline was grafted to polylactide (PLA) and BY-aniline-PLA was formulated into polymeric nanoparticles (NPs) with PLA–PEG$_{5000}$. As the BY-aniline-PLA concentration increased, the molar absorption coefficient of the nanoparticles increased linearly up to a BY-aniline-PLA to PLA-PEG ratio of 50%. The number of BY-aniline-PLA molecules per particle was then estimated from the ratio between the nominal BY-aniline-PLA concentration and the number density (or concentration) of nanoparticles evaluated by nanoparticle tracking analysis (NTA). For a BY-aniline-PLA to PLA-PEG ratio of 50%, around 3.1×10^3 BY-aniline-PLA molecules per particle were found, for a number density of 2.8×10^{16} particles/L. We reproduced this result by formulating BY-aniline-PLA-47% NPs with the same initial material concentrations. We found a number of BY-aniline-PLA molecules per particle around 7.5×10^3 for approximately half the number density (Table 1). The difference can be explained by the slightly larger diameter of our particle (~145 nm compared to ~120 nm in ref[12]). The size and number density variations might arise from the different formulation solvent. Indeed, Bodin *et al.*[12] used dichloromethane while we used chloroform to unify the formulation process with SLN formulation.

Table 1 summarises the main parameters determined by NTA. We can first notice that the number density of particles is stable and close to 10^{16} particle/L in each SLN formulation. It means that the number density is not influenced by the dye proportion. The estimated number of BY-aniline-Palm molecules per particle in SLN formulations is also given in Table 1 and ranges from 5.4×10^3 BY-aniline-Palm molecules per particle for SLN-2% to 3.2×10^5 BY-aniline-Palm molecules per particle for SLN-100%. Thus, labelling SLNs instead of PLA NPs allows us to multiply by 50 to 100 the maximum number of BY-aniline dye per particle. Indeed, the long chain length of PLA (15×10^3 g.mol^{-1}) compared to BY-aniline (790 g.mol^{-1}) limited the actual dye loading to 2.9% (w/w). BY-aniline-Palm has much lower molecular weight (1,029 g.mol^{-1}) than BY-aniline-PLA and a much greater dye loading can be achieved. One can notice that SLN-2% and PLA-47% correspond to the same quantity of BY-aniline in the formulation and yield similar number of BY-aniline per particle.

Finally, SLNs are intrinsically theranostic particles, as the prodrug DXP takes part in the formulation and is present in the core of the particle. For comparison, drug encapsulation during the formulation was not implemented for BY-aniline-PLA particles.

Table 1 – Parameters determined by nanoparticle tracking analysis (NTA) for Batch #2

NP	BY-aniline (mM)	#particles /L	#BY-aniline /particle	$\varepsilon_{particle}$ (M^{-1}.cm^{-1}) *
BY-aniline-PLA-47%	0.16	1.3×10^{16}	7.5×10^3	4.6×10^8
SLN-2%	0.16	1.8×10^{16}	5.4×10^3	2.2×10^8
SLN-25%	1.7	9.6×10^{15}	1.1×10^5	3.6×10^9
SLN-50%	3.0	1.0×10^{16}	1.8×10^5	7.7×10^9
SLN-100%	4.9	9.2×10^{15}	3.2×10^5	1.7×10^{10}

* $\varepsilon_{particle}$: absorption cross section per mole of particles expressed in M^{-1}.cm^{-1} and evaluated at the maximum absorption wavelength
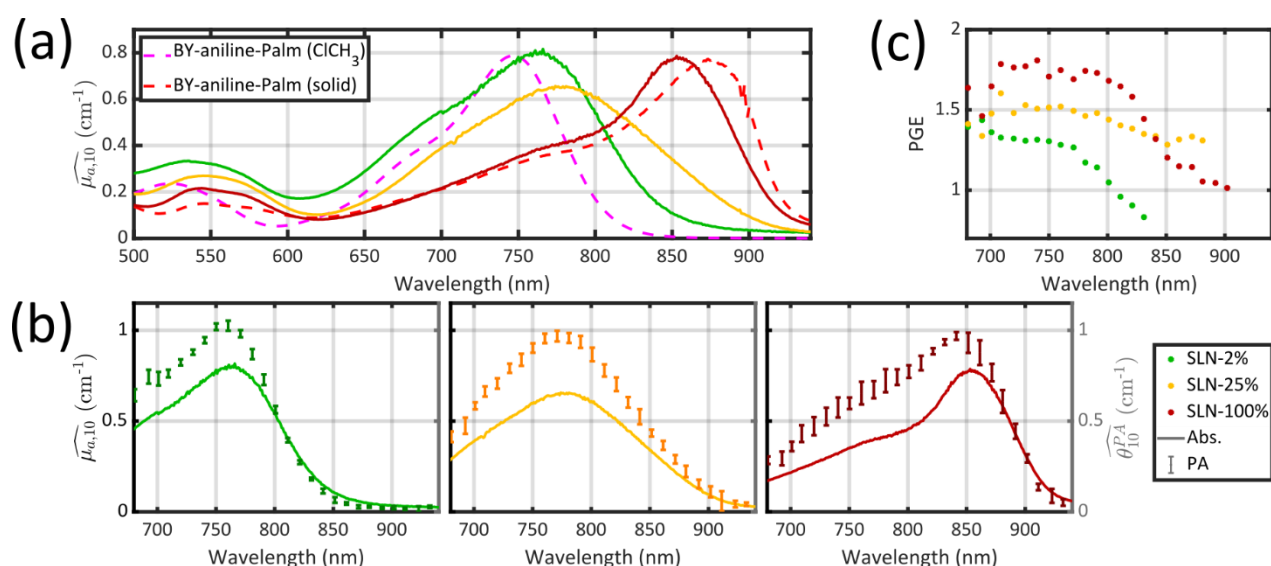
Fig. 2 – (a) Absorption spectra of SLN-2% (green), SLN-25% (yellow) and SLN-100% (dark red) compared to BY-aniline-Palm spectra in chloroform (magenta, dashed line) and in solid state (red dashed line). For the sake of readability, the absorption spectra in chloroform and in solid state were scaled to have a comparable maximum value, around 0.8 cm⁻¹. (b) Absorption (solid line) and PA (dots with error bars) spectra of SLN-2%, SLN-25% and SLN-100%. (c) Ratio between the PA coefficient and the absorption coefficient for each PA wavelength: Photoacoustic Generation Efficiency (PGE). To limit artefacts related to the ratio at low absorbances, the ratio was calculated only for absorbance and PA coefficient greater than 0.15 cm⁻¹. The colour code for SLN is applied in all the subfigures.

B.3. Characterization of optical properties of SLNs

Optical absorption properties of SLN formulations were measured by absorbance spectrophotometry in the visible and NIR range at ambient temperature. First, the BY-aniline-Palm spectrum was measured in solution (Fig. 2(a)). Chloroform was used as a solvent as BY-aniline-Palm is not hydrosoluble. No spectral difference with BY-aniline and BY-aniline-PLA in the same solvent were noticed. In the range 650-980 nm, the spectrum comprises a band around the maximum at 745 nm and a vibronic shoulder around 690 nm. Then, the absorption spectrum of the SLN formulations were acquired with a spectrophotometer equipped with an integrating sphere and compared to the spectra in solution. SLN-0% at the same dilution factor were used as a reference for the spectrometer (blank) to limit the influence of the scattering on the absorbance spectra. To avoid potential bias due to the increasing absorption of the SLN suspensions with the BY-aniline-Palm concentration, all batches were diluted in Milli-Q water to obtain a constant BY-aniline-Palm concentration (1.73×10^{-2} mM), as detailed in Table S1. Decadic absorption coefficients $\widehat{\mu_{a,10}}$ were obtained by dividing the absorbance by the length of the cuvette. The hat over the coefficient symbols indicates that the quantities are measured at the defined BY-aniline-Palm concentration. In Fig. 2(a), $\widehat{\mu_{a,10}}$ spectra reveal a progressive modification of the absorption spectrum with the increasing percentage of BY-aniline-Palm in the SLNs. For SLN-1% and SLN-2%, the spectrum is close to that of BY-aniline-Palm in solution (absorption band around 753 nm). As the BY-aniline-Palm percentage increases, the absorption band shifts gradually towards longer wavelengths and becomes more symmetrical, as shown in Fig. S11, until a new absorption band centred around 860 nm appears.

The absorption cross section per mole of particles, expressed in M⁻¹.cm⁻¹ and noted $\varepsilon_{particle}$, is defined as the decadic absorption coefficient divided by the molar concentration of particles, and is equivalent to the molar absorption coefficient for molecular dyes. Besides the bathochromic shift of the maximum absorption wavelength with the increasing BY-aniline concentration, $\varepsilon_{particle}$ evaluated at this shifting wavelength increases linearly with the BY-aniline concentration: starting from around 2×10^8 M⁻¹.cm⁻¹ for SLN-2% and reaching 2×10^{10} M⁻¹.cm⁻¹ for SLN-100% (Table 1 and Fig. S9). As a comparison, $\varepsilon_{particle}$ of BY-aniline-PLA-47% is measured equal to 5×10^8 M⁻¹.cm⁻¹, similarly to Bodin et al. [12]. Thus, $\varepsilon_{particle}$ values are consistent with the number of BY-aniline per particle. Thereby, $\varepsilon_{particle}$ of SLNs can be up to 40 times higher than for BY-aniline-PLA-47% and up to 100 times higher than the BY-aniline-PLA NPs of Bodin et al.[12] that were successfully detected with multispectral PAI in vivo. $\varepsilon_{particle}$ of SLN-100% even falls within the same order of magnitude as gold nanoparticles commonly detected in biomedical multispectral PAI such as gold nanorods, nanocubes and nanoshells[9].

The appearance of the 100-nm red shifted band (corresponding to a 1650-cm⁻¹ shift) is accompanied by several pieces of evidence pointing to BY-aniline-Palm aggregation within J-aggregates. BODIPY dyes are known to form J-type aggregates when present in a condensed form and a classical method to assess the formation of J-type aggregates is to increase gradually the water percentage in an organic dye solution[16–18]. The absorbance spectrum gradually evolves with a new band formation, very similar to the one we observed, and an isosbestic point appears. However, this method can be applied to quite amphiphilic dyes (and is applicable for indocyanine green (ICG) for instance) which is not the case of BY-aniline. No new band was observed by Bodin et al.[15] on BY-aniline spectrum in water/THF solution even at 70% water[15] and precipitation was observed for higher percentages. We therefore decided to analyse directly the solid as a reference for condensed form of BY-aniline-Palm. First, when BY-aniline-Palm is isolated and after evaporation of the organic purification solvent, the remaining solid forms flakes, suggesting a supramolecular self-organisation of BY-aniline-Palm molecules.

To follow this path, the solid-state absorption spectrum of a dried thin film of BY-aniline-Palm was measured. The spectrum is presented in Fig. 2(a) and displays a different shape than the spectrum in solution: the two bands noticed in solution (vibronic shoulder and absorption band) form a large and poorly defined band from 650 and 800 nm, and a new band is observed around 875 nm. Spectral decomposition in Gaussian function (see section D.9) allows to identify the three bands. The position and width of the new band in the solid-state spectrum are close to those observed for the 860-nm band in SLN-50% to SLN-100%. This similarity suggests that the BY-aniline-Palm molecules form the same aggregate type in the SLN-50% to SLN-100% and in the solid form, with only a more partial aggregation in the SLNs. This aggregate type has its own spectrum with a bathochromic shift, which seems to correspond, at least partially, to J-type aggregation, even if this 860-nm band is not as thin as usually observed for isolated J-aggregates[19]. Indeed, a bathochromic shift of the absorption maximum by around a hundred nanometres through the appearance of a symmetrical and thin band is among the main characteristic of J-aggregates[19]. No fluorescence exaltation was observed, either with small or large Stokes shift, as it could be the case with J-aggregates[19]. On the contrary, as shown in Fig S10, all nanoparticles were found poorly fluorescent, and this fluorescence intensity decreases even further as BY-aniline concentration increases, along with a small bathochromic effect. This decrease of fluorescence is following the aggregation-caused quenching effect proposed by Bodin *et al.*[15].

Likewise, when aggregation is perfect, an isosbestic point is generally observed between the monomer absorption band and the aggregation band. Here, it appears that the monomer band corresponding to the main S_0-S_1 transition widens before transitioning to the aggregate band. This is particularly obvious in the spectrum of SLN-25% in Fig. 2(a), which is much broader than that of SLN-2%. This could correspond to the beginning of aggregation or random aggregation. Modification of electronic levels by aggregation changes the absorption wavelengths and distorts the spectrum. Overlaid on the monomer spectrum, aggregate spectra broaden the absorption band. To clarify these phenomena and simplify the study of these spectral modifications, a spectral decomposition as a sum of Gaussian functions is presented in section B.6.

However, even though the obtained aggregation state is likely imperfect, incomplete, and somewhat random, it nonetheless remains stable over time for at least one month when stored in parafilm-sealed vial at 4°C.

B.4. Characterization of the photoacoustic properties at 25°C

Photoacoustic (PA) decadic coefficients $\widehat{\theta_{10}^{PA}}$ correspond to the optical absorption decadic coefficients, restricted to the part of the absorption converted into a PA signal[13]. They were determined using the home-made PA spectrometer described in Lucas *et al.*[13] at a temperature of 25°C. The solutions prepared for the absorption measurements (section B.3) were used for a direct comparison between the absorption and quantitative photoacoustic spectra, and because these solutions allow to operate in the same sensitivity range of the instruments for all SLNs.

First, the photostability of the BY-aniline-Palm in particles was verified. For this purpose, we used the fact that 15 sweeps of the optical wavelengths are performed consecutively for the PA spectrum measurement and we assessed $\widehat{\theta_{10}^{PA}}$ for each sweep independently. $\widehat{\theta_{10}^{PA}}$ was found constant over the 15 sweeps at the maximum absorption wavelength (Fig. S21), which indicates a photostability of the dye. Next, each PA coefficient was computed from an average over the 15 sweeps as explained in the material and method section (section D.8). Statistical analysis in the following are then performed on iterations of the measurement using the median and the MAD (cf. Material and Methods section D.8.1)).

Three typical spectra, corresponding to SLN-2%, SLN-50% and SLN-100% are displayed in Fig. 2(b), together with their respective absorption spectra. The PA and absorption spectra of SLNs exhibit similar primary trends such as the red-shift of the maximum absorption wavelength and the appearance of a new band around 860 nm for SLN-100%. However, the most striking result is that PA and absorption spectra are not superimposed for the SLNs, contrary to what is observed with a solution of nigrosine (Fig. S6) or a suspension of small (2 nm) gold nanoparticles (Fig. S20 and ref[20]). The PA spectra have significantly higher values than the absorption spectra, especially below 800 nm. PA spectra at 25°C and absorption spectra for all SLNs are displayed in Fig. S11 and Fig. S12 for Batch #1 and Batch #2, respectively.

To analyse the difference between the absorption and PA spectra, one should recall that the measured PA coefficient $\widehat{\theta_{10}^{PA}}$ is related to the decadic absorption coefficient $\widehat{\mu_{a,10}}$ by the following formula:

$$\widehat{\theta_{10}^{PA}}(\lambda) = PGE(\lambda) \cdot \widehat{\mu_{a,10}}(\lambda) \tag{1}$$

where λ is the optical wavelength and $PGE(\lambda)$ is the photoacoustic generation efficiency, defined in Material and Methods section D.8.2). Therefore, we compute $PGE(\lambda)$ for each formulation and each wavelength, by evaluating the ratio between the PA and absorption coefficients. Fig. 2(c) show that not only $PGE(\lambda) \geq 1$ over the whole spectral range (with the exception of SLN-2% above 800 nm), but also the PGE is wavelength-dependant with a maximum between 700 and 800 nm. At the maximum absorption wavelength of SLN-2%, $PGE(760 \text{ nm})$ is increasing with the BY-aniline concentration, from 1.3 for SLN-2% to 1.7 for SLN-100%. However, the global photoacoustic efficiency (GPAE), which represents the weighted average of the PGE over the whole studied range with weight equals to the optical absorption (as defined by Bodin *et al.*[15] and in the Material and Methods section D.8.2)), is globally constant 1.36 ± 0.08 (mean ± std) for Batch #1 (Table S4). This implies a strong spectral variation of PGE which will be analysed per absorption band in section B.6 with a Gaussian spectral decomposition.

In the next section B.5, we discuss the reasons that can explain the PGE above 1 for the SLNs.

B.5. Effect of the SLN matrix on the photoacoustic generation efficiency

B.5.1) Discussion on $PGE \geq 1$

While the difference between PA and absorption spectral shapes would have been noticeable with spectra in arbitrary units, the evaluation of $PGE(\lambda) \geq 1$ is made possible by the remarkable quantitative characteristic of the PA spectrometer, which is provided by its calibration[13] (cf. Material and methods section D.8). A PGE greater than 1 is a rather surprising finding for dilute aqueous suspensions. Indeed, in the literature employing calibrated photoacoustic spectrometer, PGE was determined inferior or equal to 1 for molecular absorbers in water. In particular, PGE is found inferior to 1 for fluorescent molecules since fluorescence is a competitive deexcitation pathway[21,22]. For small gold particles, PGE was found equal to 1[20,21]. PGE was also found equal to 1 for semiconducting polymer nanoparticles[23]. Similarly, PGE of BY-aniline-PLA 47% was found close to 1 (Fig. S13 and Bodin *et al.*[15]).

To understand the observed PGE values above 1, we need to go into further detail on the PGE. The measured PGE is the product of the photothermal conversion efficiency (PTCE) and the effective Grüneisen coefficient of the solution relative to water[13,22] . The PTCE represents the conversion efficiency of absorbed energy to prompt heat. Thereby, PTCE ≤ 1 to respect the law of conservation of energy. The Grüneisen coefficient describes the conversion of heat energy to acoustic pressure. The evaluation relative to water here is linked to the calibration process. Thereby, PGE can be expressed as:

$$PGE(\lambda) = PTCE(\lambda) \cdot \frac{\Gamma_{\text{sample}}(\lambda)}{\Gamma_{\text{water}}} \qquad (2)$$

where Γ_{sample} is the effective Grüneisen coefficient of the sample solution and Γ_{water} is the Grüneisen coefficient of water. The Grüneisen coefficient of water is temperature-dependent but it is independent of the excitation wavelength. This formula assumes thermal and stress confinements, which are both respected at the spatial scale of the sample container. Having PGE > 1 implies that $\Gamma_{\text{sample}} > \Gamma_{\text{water}}$. It is worth noting that the $PGE(760 \text{ nm})$ increases with the BY-aniline percentage while the dilution of the SLN suspensions in water increases by a factor 31 between the suspensions of SLN-2% and SLN-100%. Therefore, unformulated reagents in the continuous phase (water) are unlikely to be responsible for PGE > 1. However, the Grüneisen coefficient of water is around 0.12 at 25°C while it varies between 0.5 and 1.1 for lipids[24]. In case of thermal and stress confinements at the scale of a single SLN particle during the laser pulse excitation, the photoacoustic generation would mainly occur inside the nanoparticle and the ratio $\Gamma_{\text{sample}}/\Gamma_{\text{water}}$ would be on the order of 4 to 10. However, with a laser pulse duration of $\tau_p \sim 7 \, ns$ and a spherical particle radius $R \sim 50 \, nm$, the stress confinement condition is not verified at the spatial scale of the particle and the thermal diffusivity in the surrounding medium cannot be neglected during the laser pulse. To limit the particle radius to the optically absorbing core, R was taken smaller than the hydrodynamic radius and on the

order of the size observed on the TEM images (Fig. 1(d)). The thermal diffusivities in solid palmitic acid[25], in PLA[26] and in water are on the order of $\chi \sim 10^{-7} \, m^2.s^{-1}$, which implies that the heat diffusion length in these materials is about $L_{th} \sim 2 \cdot \sqrt{\chi \cdot \tau_p} \approx 50$ nm. L_{th} cannot be considered small compare to the size of the particle, which implies a significant thermal diffusion in the surrounding water during the laser excitation. But L_{th} is also not large compared to R so the particle experiences a partial thermal confinement during the laser pulse. The interparticle distance for SLN-2% can be estimated on the order of 800 nm (3 µm for SLN-100%) and is much larger than $L_{th} + R$, therefore the particles can be considered isolated and synergistic effects between particles can be excluded. A 50 nm-thick heated layer of water around the particle implies a volume about 7 times larger for this layer than for the particle itself and suggests a significant contribution of this water layer to the photoacoustic signal and therefore to Γ_{sample}. One can then understand why the measured PGE is not larger than 2.

Assuming a perfect thermal contact between a single spherical particle and its surrounding water, the characteristic time for heat exchange[27] is $\tau_E \sim \rho_{NP} \cdot C_p^{NP} \cdot R^2 / (3 \cdot k_{water})$ where ρ_{NP} and C_p^{NP} are the density and the specific heat capacity of the particle respectively and k_{water} is the thermal conductivity of water. Interestingly, this formula depends on the parameters of both the nanoparticle and the surrounding medium. For SLN and PLA particles, $\tau_E \sim 2 \, ns$ when taking the parameters for solid palmitic acid[25] and PLA[26,28]. $\tau_E < \tau_p$ confirms the partial confinement of the heat inside the particle. It worth noting that τ_E depends quadratically on the radius of the particle. For much smaller particles, such as the gold nanoparticles used here as a reference ($R \sim 1 \, nm$), one can have $\tau_E \ll \tau_p$ meaning that the particle is mostly a heat source for the surrounding water. For these gold particles, the PGE was found equal to 1[20].

Nanoparticles with a PGE larger than 1 were also observed by Aoki et al.[29] but the PGE was not evaluated quantitatively. In their study, polymer nanoparticles (PNP) containing an organic dye were exposed to laser pulses with $\tau_p \sim 1 \, ns$. Similarly to our study, the thermal diffusivity of the polymer materials were on the order of 10^{-7} m².s⁻¹, but because of the shorter pulse duration $L_{th} \approx 20 \, nm$. They demonstrated that the photoacoustic signal arose almost entirely from the water for small particles (radius ~ 20nm, $\tau_E \sim 0.3 \, \tau_p$) and a significant contribution of the particle to the photoacoustic signal could be observed for larger particles (radius ~ 60 nm, $\tau_E \sim 3 \, \tau_p$) and increased with the particle radius. Polymers with Grüneisen coefficients ranging from 0.7 to 1.4 at 20°C were used for the PNP synthesis and the photoacoustic signal generated by the solutions increased with the Grüneisen coefficient for the larger particles while it remained constant for the smaller ones. The PGE above 1 was attributed to a partial thermal confinement inside the larger PNPs and to the large Grüneisen coefficient relative to water of the matrix polymers.

Here, we compare PLA particles loaded with BY-aniline-PLA and SLN loaded with BY-aniline-Palm, that have similar hydrodynamic size and thermal properties. To compare particles with a similar dye loading and concentration (Table 1)
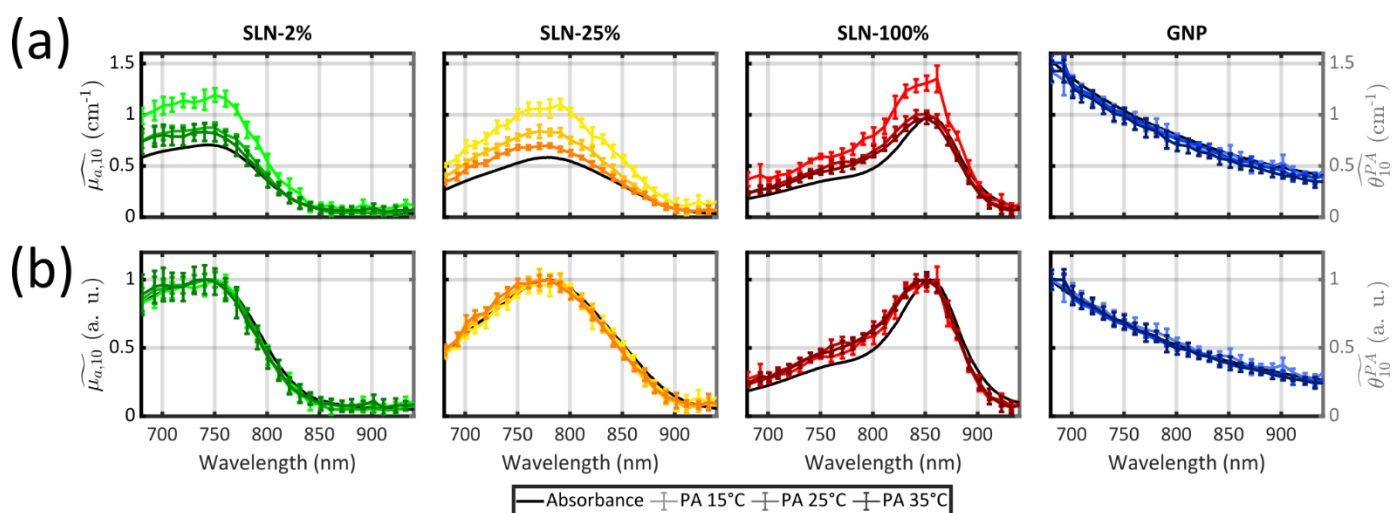
Fig. 3 – (a) Absorption spectra (black) and PA spectra at three temperatures (15°C, 25°C and 35°C) of SLN-2% (shade of green), SLN-25% (shade of yellow), SLN-100% (shade of red) of Batch #2, gold nanoparticles (shade of blue). (b) Absorption spectra (black) and PA spectra at three temperatures (15°C, 25°C and 35°C) normalized by the spectrum maximum. The colour code is the same as in (a).

we compare SLN-2% and BY-aniline-PLA-47%. The fluorescence can be considered negligible for the two particles, leading to PTCE ≈ 1. The particles are therefore expected to experience similar partial thermal confinement inside the particle and to generate a similar heating of the surrounding water layer. At 25°C, we determined GPAE = 1.05 for BY-aniline-PLA-47% and GPAE = 1.2 for SLN-2% (Table S4). The Grüneisen coefficient of PLA was not found in the literature. However, the large Grüneisen coefficient of lipids relative to water can explain PGE>1.

Theoretical considerations and comparisons with other experimental studies strongly suggest that the solid lipid matrix of the particle is responsible for PGE>1. Numerical simulation of the photoacoustic generation for the particle would require the determination of several thermodynamic and acoustic parameters of the different materials composing the particle and the implementation of a complex model[30], which are beyond the scope of our experimental study. However, following the approach of Aoki et al.[29] and Simandoux *et al.* [31], we further demonstrate that PGE is linked to the matrix of the particle by investigating the PA emission of the particles at different water temperatures. The Grüneisen coefficient of water is temperature-dependant, and the Grüneisen coefficient of the lipid core is not expected to vary in the same proportion[24] in the range 15°C to 35°C. Therefore, the effective Grüneisen coefficient should manifest a dependence on the temperature only if the lipid core is involved in the photoacoustic signal generation.

B.5.2) Photoacoustic coefficient at different temperatures of SLN-2% and PLA-47%

In this section, we perform a comparative study of PGE values evaluated for SLN-2%, PLA-47% and gold nanoparticles (GNP) at different temperatures: 15°C, 25°C and 35°C. The temperature dependence of PGE was investigated for all SLNs of Batch # 2, but for the sake of clarity, the results are presented in section B.6 together with a discussion on the band-dependence of PGE.

First, at the laser fluence and ultrasound frequencies involved in this study, we consider that thermal nonlinear contributions to the photoacoustic signal are negligible and cannot explain PGE > 1. Indeed, the PA coefficient was not enhanced at higher fluence for SLN-2% (Fig. S22). Thereby, the Grüneisen coefficient of the water layer surrounding the particle is expected to be determined by the temperature of the thermostatic water tank in which the sample containers are immersed. The temperature of the water tank was set successively at three different temperatures: 15°C, 25°C and 35°C and quantitative PA spectra were acquired. The Grüneisen coefficient of water increases from 0.07 to 0.18 in this temperature range[24].

All previous measurements with the photoacoustic spectrometer were performed at a fixed temperature[12,13,15,20]. To obtain, for the first time, quantitative PA spectra of the same sample but at different temperatures, we determined that the calibration process needed to be repeated for each temperature. Thereby, computed PGE values are relative to water at the same temperature. The absorbance spectra of the three samples were found independent of the temperature (Fig. S19 and S20). Validation of our experimental method was performed using the suspension of small GNPs. Indeed, the photoacoustic generation of these GNPs arises from the surrounding water[32] and, as a consequence, the calibrated PA spectrum is expected to match the absorption spectrum for all temperatures. The superimposition is verified visually (Fig. 3) and by a GPAE on the order of 1 for the three temperatures (Table S5).

Following this validation, the quantitative PA spectra of SLN-2% and PLA-47% can be compared. The first result common to the two particles is that the spectra at the three temperatures are not superimposed although their spectral shape is conserved. Normalisation to the maximum value shows that the spectra differ by multiplicative factors. These factors are given by the GPAE (Table S5). The GPAE increases with the decreasing temperature, that is to say with the decreasing Γ_{water}. While Γ_{water} decreases, one can hypothesise that the relative weight

of the heated water layer to Γ_{sample} would decrease and thereby the relative weight of the particle would increase. However, the PA spectra at 25°C and 35°C are almost superimposed indicating that $\Gamma_{\text{sample}}/\Gamma_{\text{water}}$ is nearly constant between the two temperatures while Γ_{water} increases from 0.12 to 0.18. On the contrary, the PA coefficients were found larger at 15° than at 25°C with GPAE(15°C)/GPAE(25°C) = 1.38 for SLN-2% and GPAE(15°C)/GPAE(25°C) = 1.18 for PLA-47%, while $\Gamma_{\text{water}}(15°C) = 0.06$ and $\Gamma_{\text{water}}(25°C) = 0.12$. Aoki et al.[29] demonstrated the contribution of the particle to the photoacoustic signal by further decreasing the water temperature down to 4°C where $\Gamma_{\text{water}}(4°C) = 0$. However, the calibration of our photoacoustic spectrometer would have not been possible in this condition which is why we limited our investigations to 15°C for this first exploration of the spectrometer performance at different temperatures. The larger difference in the PA coefficient values when the temperature was set below the ambient temperature of 25°C than when it was set above may indicate a saturation process or a limit. This result is observed for all the other SLNs of Batch #2 (Fig. 3). Measurements at more temperatures, especially below 25°C, are beyond the scope of this study but will be investigated in future studies to better understand the variations of $\Gamma_{\text{sample}}/\Gamma_{\text{water}}$ with the water temperature.

The significant increase of the PA coefficient at 15°C for the SLN particle is an additional argument that the particle matrix is involved in the photoacoustic generation. The higher GPAE values for SLN-2% than for BY-aniline-PLA-47% is further evidence that the Grüneisen coefficient of the solid lipid core is larger than the polymer one.

B.6. Per-band analysis of the absorption and PA spectra and PGE

While PGE values above 1 could be explained by the lipid matrix of the SLN particles in section B.5, the wavelength-dependency of PGE, especially for SLN-50% to 100%, requires further investigations. Band-dependent PGEs have been reported for fluorescent dyes in solution. The poor dye solubility in water leads to a mix of different species (monomers and aggregates) that exhibit different absorption bands with various photoacoustic properties[22].

In this section, we perform a per-band analysis of the absorption and PA spectra, and subsequently of the PGE. The decomposition of the spectra in three absorption bands and the derived Band PhotoAcoustic Efficiencies (BPAE) are first presented. Then, each band is attributed to an energy transition or species. Finally, further investigations of the band-dependant PGE are exposed.

B.6.1) Spectral decomposition of the absorption and photoacoustic spectra at 25°C

To reduce the complexity of the spectral analysis, we decomposed $\widehat{\mu_{a,10}}$ spectra, in the range 640- 980 nm, and $\widehat{\theta_{10}^{PA}}$ spectra (at 25°C), in the range 680- 930 nm, as the sum of three Gaussian functions. A simpler Gaussian decomposition of both absorption and photoacoustic spectra, with only two Gaussian functions, had been performed previously on BY-aniline-PLA
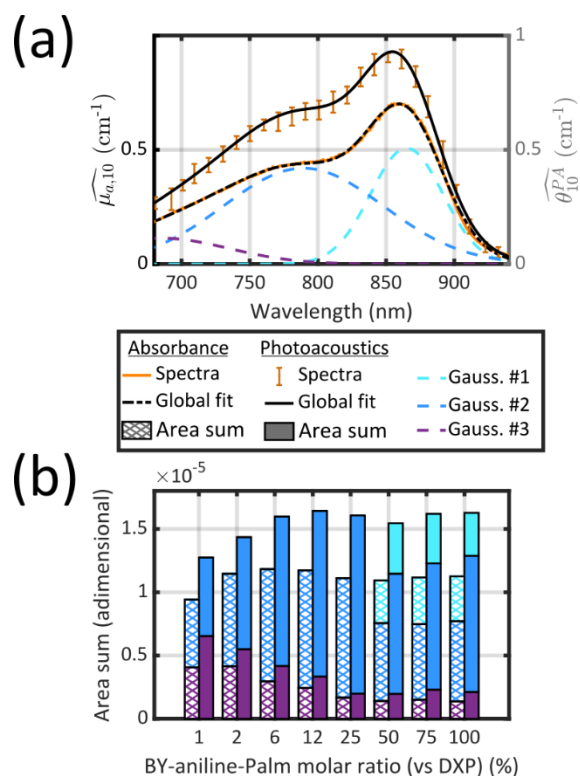

Fig. 4 – (a) Decomposition of the absorption spectrum for SLN-75% in the sum of three Gaussian functions. From left to right, the Gaussian functions are centred at 685 nm (purple), 789 nm (blue) and 865 nm (cyan). The sum is given in black dotted line. For sake of readability, only the PA spectrum (with error bars) and its global fit (in black continuous line) are shown. For details see Fig. S14 and Fig. S15. (b) Contribution of each Gaussian function (area) in the total spectrum area for each SLN. Absorption spectra are on the left-hand side in hatched bars while PA spectra are on the right-hand side in coloured bars. The colour code is the same as in (a) and we are considering Batch #1 (for Batch #2, see ESI).

particles[15] and showed the feasibility of such decomposition for BY-aniline and its interest for band analysis. This decomposition was reproduced here for BY-aniline-PLA-47% (Fig. S18 and Table S3). Within a complete study including various concentrations, PA spectra at different laser fluences as well as ns-transient absorption measurements, the decomposition in two bands mainly allowed to highlight a ground state depopulation phenomenon in one of the two bands.

The three Gaussian functions are ordered by decreasing centre wavelength and named Gaussian #1 to Gaussian #3. Pure BY-aniline-Palm spectra in chloroform and in solid state were first decomposed as illustrated in the material and method section D.9. The width and the centre wavelength of Gaussian #1 evaluated from the Gaussian decomposition of the solid-state spectrum and the centre wavelength Gaussian #3 evaluated from the solution spectrum were used as references for the Gaussian decomposition of the SLN suspension spectra. Moreover, the centre wavelength and the width of Gaussian #2 and the width of Gaussian #3 were jointly optimized for the absorption and PA spectra of SLN suspensions. Amplitudes were optimized independently. Fig. 3(a) illustrates that the Gaussian decomposition enables a satisfactory fit of both the absorption and the PA spectra. The quality of the decomposition was verified for all the formulations as shown in Fig. S14 and Fig. S15 for Batch #1 and in Fig. S17 for Batch #2. Detailed results of the model fitting parameters are given in Table S2 for Batch #1 and in Table S3 for Batch #2.

It is remarkable that despite the spectral deformation between the PA and absorption spectra, they could be both decomposed with the same three Gaussian functions by mainly varying the weighting factors. For the rest of this study, we will only use these 3 bands, which are sufficient to describe the spectrum instead of the 30 wavelengths. To consider both the amplitude and the width of each band, we compute the area of each Gaussian. Those areas allow to compare the weight of each band in one formulation, and also to evaluate the weight of each band in relation with the BY-aniline percentage. The computed areas are displayed in a vertical stacked bar chart in Fig. 4(b). This figure focuses on Batch #1, but an equivalent figure is given in ESI for Batch #2 (Fig. S16). The first striking observation is that besides the spectral transformation, the total area (sum of the areas for the three Gaussian functions) is constant for the $\widehat{\mu_{a,10}}$ spectra, and constant and 1.4 times higher for the $\widehat{\theta_{10}^{PA}}$ spectra for BY-aniline-Palm percentage above 6%. The constant total areas imply an interplay and a balance between the absorption bands. For $\widehat{\mu_{a,10}}$, the purple band (Gaussian #3) represents around 50% of the total area for SLN-1% and gradually diminishes to reach a plateau around 15% from SLN-25%. The blue band (Gaussian #2) first increases with the BY-aniline-Palm percentage, reaching 85% of the total area for SLN-25%. From SLN-25%, it gradually decreases, while the cyan band (Gaussian #1) appears. To compare absorbance and PA spectra, we use here the Band PhotoAcoustic Efficiency (BPAE) defined by Bodin et al.[15] as the ratio of the areas of each band between the photoacoustic spectrum and the absorption spectrum (cf. Material and Method section D.9). It corresponds to a weighted mean PGE on the band. The results are presented in Table S2 and Table S3. For the BPAE of Gaussian #3, no real trend seems to emerge with values about 1.3. The BPAE of Gaussian #1 is remarkably stable with a value around 1. On the other hand, for Gaussian #2, the BPAE increases with the BY-aniline-Palm ratio, between 1.2 for SLN-1% and 1.7 for SLN-100%.

Despite some differences in the distribution of areas between the bands, very similar trends and values are observed in Fig. S16 for Batch #2.

B.6.2)   Attribution of the three absorption bands

The Gaussian decomposition of absorption spectra was previously reported for molecular dyes (ICG[33,34], Methylene blue[35] and IR775 dye[36]) and allowed to differentiate bands associated with monomeric and aggregated forms[33,35], to distinguish contributions from different vibrational states[35,36], or even to assess variations in spectra caused by the addition of another compound such as a drug[34].

The Gaussian functions of Fig. 4 can be interpreted in terms of different transitions. Gaussian #3 (purple) models the shoulder (a priori S_0-S_1 vibronic state transition[37]), which is mostly visible at BY-aniline-Palm percentage below 6% as illustrated in Fig. S14. Gaussian #2 (blue) is centred around 760-800 nm and could corresponds to S_0-S_1 0-0 electronic excitation[37], which is the main absorbing band in chloroform. These two bands were also identified in polymer particles with BY-aniline-PLA studied in Bodin et al.[15] and in BY-aniline-PLA-47% (Fig. S18). The enlargement and the bathochromic shift of Gaussian #2 in SLNs, when the BY-aniline-Palm percentage increases, could be explained by the gradual environment change for BY-aniline. Indeed, solvatochromism experiments in Bodin et al.[15] showed that the absorption spectrum of BY-aniline changes with its environment polarity. Strong bathochromic and hypsochromic shifts of the band maximum were observed depending on the polarity of the solvent: from 728 nm in cyclohexane to 772 nm in DMSO. As the BY-aniline-Palm percentage increases in SLNs, the environment polarity of BY-aniline is necessarily modified, as aromatic rings become more numerous and interact with each other. For low concentrations of BY-aniline-Palm, each BY-aniline-Palm molecule is expected to mainly interact with aliphatic chains (typically from DSPE or palmitate from DXP), whereas interactions with aromatic rings should increase with the increasing number of BY-aniline-Palm per particle even when structured aggregates are not formed. Random aggregation could also cause the band enlargement. Gaussian #1 (cyan) appears only for BY-aniline-Palm percentage above 25% and models a new band with a 100-nm (or 1650-cm^{-1}) bathochromic shift with regards to SLN-1%, likely corresponding to partial J-type aggregation of BY-aniline[19].

The attribution of the absorption band gives indications that compare to the low BY-aniline concentration in PLA particles, for which the weight of the vibronic shoulder and S_0-S_1 0-0 electronic transition remained stable while the dye concentration increased, the high concentration in the SLN particles strongly impact the weight of the vibronic shoulder and S_0-S_1 0-0 electronic transition. This impact suggests strong intermolecular interactions and coupling between the BY-aniline, up to the formation of J-aggregates.

Surprisingly, the band associated with the J-aggregates has a lower BPAE than the two other bands. Moreover, the BPAE is around 1 at 25°C and this value is also observed for GNP for instance. In previous studies[15,22], reported BPAE involved fluorescent dyes and the band-dependency of the PGE was attributed to a band-dependant PTCE. Additionally, the BPAE was below 1 because of the quantum yield and the energy 'stored' in exited states with life times on the same order of magnitude or larger than the laser pulse duration could further lower the PTCE.
Since the BPAE is larger than 1 and because a very weak fluorescence was recorded (Fig. S10) even for low BY-aniline concentration, we investigate independently the possibility for band-dependant effective Grüneisen coefficient and a band-dependant PTCE.

B.6.3)   Photoacoustic coefficient at different temperatures

We formulate the hypothesis that the effective Grüneisen coefficient might be different for the different absorption bands. In other words, variation of the BPAE would imply different relative contribution of the particles and their surrounding water layers to the photoacoustic signal. Following

this idea, a BPAE = 1 at 25°C for the J-aggregate band would suggest an enhanced energy transfer to water for this band.

To test this hypothesis, we measured PA spectra at three different temperatures: 15°C, 25°C and 35°C for the SLNs of Batch #2 (Fig. 3 and Fig. S19 for SLN-50%). The temperature variation allows to modify the relative contribution of water. Moreover, the three temperature absorption spectra were performed (Fig. S19), with no significant changes. DLS measurements at three temperatures were also performed, as object size can influence thermoelastic expansion[29]. A small decrease of the size was noticed at 15°C (about 5%) but should not significantly change the thermal behaviour.

The results for SLN-50% an SLN-100% at 15°C showed that the BPAE for the J-aggregate band could reach 1.5 and 1.2, respectively, which indicates that the BPAE for this band is not limited to 1 and that the particle matrix has a contribution to the photoacoustic signal for this band. More globally, one can clearly observe that the PA coefficients increase with the decreasing temperature for all the particles (Fig. 3(a)). However, for each formulation, PA spectra at the different temperatures superimpose when normalized to the maximum value (Fig. 3(b)). This implies that the PA spectral shape is independent of the temperature. Thereby, for each SLN, the 2 or 3 different BPAEs varies as the GPAE. The relative variation of the BPAE at 15°C and 35°C compared to 25°C is therefore not influenced by the BPAE value at 25°C. As a consequence, the relative contribution of the particles and their surrounding water layers does not depend on the absorption band, which invalidate the hypothesis of a band-dependant effective Grüneisen coefficient. Thereby, the effective Grüneisen coefficient is constant over the entire spectra. We have demonstrated that PGE is larger than 1 due to a thermoelastic expansion of the SLN matrix, but the per-band variability of PGE should be attributed to light to heat energy conversion.

The relative change of the GPAE with the temperature were found to be dependent on the BY-aniline-Palm concentration for Batch #2 (Table S5). However, the small number of water temperatures, batches and BY-aniline-Palm concentrations do not allow to speculate on trends.

B.6.4) Spectral variation of the photothermal conversion efficiency

Because of the very weak fluorescence of the SLNs, the fluorescence quantum yield cannot explain the significant variations in the BPAE values observed between the different bands and for Gaussian #2 with the BY-aniline-Palm percentage. However, PAI is sensitive to the conversion of optical energy in prompt heat, which means that the PTCE could be reduced by a photochemical decay pathway or by the transient energy storage during the laser pulse excitation in long-lived excitation states such as a triplet state.

Stability of the PA signal over the sweeps in Fig. S21 indicates that the photochemical pathway is unlikely. For BY-aniline-PLA, Bodin et al.[15] show that long lifetime excited states leading to ground state depopulation were responsible for a decrease of the PA signal especially at BY-aniline-PLA

percentage below 50%. As SLN-2% have the same number of BY-aniline per particle as BY-aniline-PLA-50%, the ground state depopulation is expected to be limited for the SLN investigated here. A ground state depopulation would depend on the deposited optical energy and would result in a PTCE decreasing with the laser fluence. In addition to the measurements perform with the laser fluence of ~3.5 mJ.cm^{-2}, we measured the calibrated PA spectrum with a laser fluence of 2.5 mJ.cm^{-2} (Fig. S22). For SLN-25% and SLN-100%, the difference between the two spectra is not significant, and the PGE is not lower for the higher fluence, especially for the J-aggregates band which has a lower BPAE.

Additionally, we investigate the presence of triplet states and long lifetime non-radiative pathways in SLNs using transient absorbance spectroscopy with nanosecond pulses. In this spectroscopic technique[38], a nanosecond pump laser is used to achieve an excited state of the molecule, whose spectrum is measured by a probe light beam, similarly to a spectrophotometer. The wavelength of the pump laser was set equal to 680 nm, which was the maximum wavelength available for the apparatus we used. Such spectroscopic system is homebuilt and somewhat unique. The spectrum obtained without the pump laser is subtracted from the one obtained with it to identify absorption variation between fundamental and excited states. For a wavelength of this subtracted spectrum, a positive signature means that the excited state absorbs more than the ground state, and a negative signature indicates the opposite (referred to as bleaching). The spectrum can be measured at different times after excitation to determine the decay lifetime and the de-excitation rates of the excited species. With a pump at 680 nm, we expect to probe the excited states linked to the S_0-S_1 0-0 electronic transition band. The S_0-S_1 vibronic state transition band cannot directly yield long-lived states.

Before focusing on SLNs, the transient absorption spectrum of BY-aniline-Palm in DCM was measured (Fig. S23) and showed that the excited state goes back to the ground state in around 5 ns. This results is similar to the results of Bodin et al.[15] on BY-aniline, but we found a shorter excited state lifetime for the grafted dye (~ 5 ns compare to a few tens of nanoseconds). Regarding SLN-2%, we observe a disappearance of the positive and negative signatures in a few nanoseconds after the laser excitation and lower transient absorption values compared to BY-aniline-Palm in DCM, as shown in Fig. S23. Given the very short de-excitation times, the signal was disrupted by the presence of fluorescence. Therefore, a measurement of the spectrum without a source beam was performed to correct the signal for fluorescence. For SLN-25% and SLN-100%, the subtraction of the excited/non-excited spectra has even smaller values and the difference can be considered negligible even at 0 ns delay between pump and probe. Therefore, no energy storage should hinder the PA generation for SLNs with a BY-aniline-Palm ratio higher than 25%. Furthermore, bubbling with inert gas (argon) for 10 minutes did not change the transient spectroscopic signal, indicating the absence of triplet state species for the excited band.

A decrease of the excited state lifetime with the increasing concentration of BY-aniline-PLA was already noticed by Bodin *et al.*[15] for PLA particles and was associated with a decrease in the fluorescence quantum yield and an increase of the PGE. For SLNs, the BPAE of Gaussian #2 increases from SLN-2% to SLN-25%. However, no saturation of this BPAE was observed for higher concentrations for Batch #1. Therefore, the reduced lifetime of the excited state and the weaker fluorescence signal may only partially explain the BPAE increase with the increasing BY-aniline-Palm concentration for this band.

Unfortunately, the upper wavelength of the pump laser at 680 nm did not allow for a direct excitation of the aggregation band, and no undirect excitation was noticed. Therefore, we could not evaluate the existence of longer-lived excited species in this band, nor explain the lower BPAE for Gaussian #3. Extension of the wavelength range of the nanosecond-transient absorption spectrometer requires significant investments and could not be performed for this study.

C. Discussion

The goal of this work was to create new theranostic agents for photoacoustic imaging and to characterize their spectral properties and efficiency as imaging agents. Using a BY-aniline compound grafted on a palmitate chain, we have formulated the first solid lipid nanoparticles tailored for PAI, employing a straightforward and one-step formulation process. The exquisite and versatile dye loading capability enabled us to increase of the per-particle absorption with small modifications of the particle size. Interestingly, we succeeded in formulating SLNs with up to 100% BY-aniline-Palm. In absence of the prodrug, SLN-100% can be considered as pure contrast agents. The interchangeability of the dye and the prodrug is certainly due to the identical palmitate grafting. From the application perspective, for percentages above 50% SLNs can be considered as dominantly contrast agents while below 50% they are dominantly drug carriers. No toxicity tests or animal injections were performed so far. However, DXP-loaded SLNs[2] and PLA nanoparticles[12] containing BY-aniline were not toxic to cells up to a particle concentration of about 0.45 mg/mL . Furthermore, PLA particles were visible in photoacoustic imaging[12] and accumulation of SLN in arthritic paws of mice was confirmed with fluorescent contrast agents[2]. We can be confident that these SLNs will be detectable and usable in multispectral photoacoustic imaging (PAI) in vivo. The determined absorption cross section per mole of particle place the high loaded SLNs in the same range as gold particle commonly used for biomedical preclinical imaging studies[9].

The quantitative characteristic of the PA spectrometer allowed us to observe that the photoacoustic efficiency is higher for the SLN suspensions than for an aqueous solution of molecular compound with the same absorption. The novel approach of acquiring calibrated PA spectra at three different temperatures enabled us to demonstrate that the enhancement of the PGE was indeed linked to a partial expansion of the lipid matrix coupled with the expansion of the surrounding water layer. This demonstration highlights that, in addition to the absorbing molecule, the material of the nanoparticle may play an important role in the design of organic particles for PAI, especially for material with a Grüneisen coefficient much higher than water.

The paired optical and PA spectra revealed spectral transformation with the increasing BY-aniline-Palm concentration, and a band-dependency of the photoacoustic efficiency. The fact that the PA and absorption spectral shapes are not always superimposed, even after correction for scattering, showed the importance of an upstream characterization of the nanoparticle. Indeed, considering the accurate PA spectrum of a contrast agent may prove crucial for its discrimination from endogenous absorbers and for the quantitative evaluation of its distribution in multispectral PAI. The concern regarding the upstream PA characterisation of contrast agents rather than relying only an optical absorbance spectrum was already shown for molecules[22], and we highlight here that it is all the more required for nanoparticular agents. With the three-temperature approach, we were able to show, that the spectrum distortion was necessarily linked to per-band variations in the energy conversion between light and prompt heat and not to spectral variations in the thermoelastic expansion. Despite our attempt to understand the band-dependant photothermal conversion, we were not able to determine the associated photophysical phenomenon. PA spectra at different light fluences and transient absorption spectra could not reveal long lifetime excited state that could result in a ground state depopulation. However, reporting our findings and investigations is of strong interest since similar behaviour may occur in different nanoconstructs for PAI.

Regarding the spectral transformation, we demonstrated that both absorption and PA spectra could be interpreted as a balance between two different bands at low concentration of BY-aniline-Palm and three different bands at high concentration of BY-aniline-Palm. The absorption band centred at 860 nm (corresponding to Gaussian #1) was attributed to the generation of J-type aggregates. The aggregation phenomenon, particularly J-type aggregates, is sought after by various research teams working in the development of PAI contrast agents. Indeed, J-aggregation can increase the molar absorption of a compound with a great compacity and often improves the photostability[19,39]. Moreover, the red-shifted maximum absorption wavelength allows to use higher excitation wavelengths for a better penetration in biological tissues and the usually observed thin absorption band facilitates the separation from endogenous absorbers with spectral unmixing algorithms. Enhanced fluorescence is not desired, as a competitive deexcitation pathway, but is not systematic with J-aggregates, especially if aggregation is imperfect. Indeed, random molecule organization in aggregates can even lead to a reduction in fluorescence through the effect of aggregation caused quenching[15]. For instance, here, no fluorescence was recorded at high concentration in BY-aniline-Palm. The formulation principle with dye aggregates generally relies on pre-aggregation by progressive evaporation of the organic phase followed by inclusion of the aggregates in nanovectors. For example, aggregates can be inserted into a lipid film

subsequently formulated into liposomes[40] or they can be encapsulated after the liposomes formulation[41]. Pre-formed aggregates can also be included by a double emulsion process[42,43]. Another aggregation method relies on the maturation of dye-loaded particles either by waiting a long period of time (about 60 days for PAtrace[44]) or by favouring molecular interactions (reduced pore spaces, addition of metal ions, etc.)[45]. All these processes allow for aggregation of quality but requires a very long preparation time and/or numerous steps. Moreover, it is difficult to control the quantity of formed aggregates and to halt the aggregation process. With the SLN formulation presented here, aggregation occurs in situ for sufficient BY-aniline-Palm concentration, and in less than 4 hours, the nanoparticles can be used. We evaluated the potential maturation of the J-aggregates after long term conservation (3 months). We observed the appearance of large crystallized objects in the suspension but optical spectra were similar to fresh suspensions with no enhancement of the optical absorption around 860 nm compare to 760 nm. With BY-aniline-Palm and our one-pot rapid SLN formulation, the appearance of perfect J-aggregate was not shown. The J-aggregation did cause a red-shift of the maximum absorption wavelength beyond 800 nm which is interesting from a detection perspective in biological tissue[9], but no superior enhancement of the absorption or PA cross section per mole of particles was observed. Moreover, the absence of a perfect control of aggregation level, as opposed to long maturation processes[44] and as seen in batch-to-batch comparison, requires an absorption and PA spectral characterization of each batch. However, the stability over time of the absorption and photoacoustic spectra, make it possible to use a batch at least for a month when stored at 4°C.

Despite the simplicity of the nanoparticle formulation proposed here and the excellent dye loading capabilities of the SLNs, the use of BY-aniline revealed complex photophysical phenomena in addition to the surprising PA properties such as a PGE superior to 1. This complexity was found to be linked to the aggregation properties. Solid-state absorption spectrum indicates similar J-type aggregation in BY-aniline-Palm solid. The supramolecular arrangement in solid results in flakes. Moreover, TEM images of SLNs showed facetted surface and less spherical particle as the BY-aniline proportion increases. The spatial arrangement of the structured aggregates in the SLNs and the nanostructuration of the particles could be of interest to better understand the particular properties of BY-aniline-Palm SLNs. The current study demonstrated the strong involvement of the lipid matrix in the PGE value. Indeed, the comparison of SLN-2% and BY-aniline-PLA-47%, which contain the same concentration of BY-aniline but have different matrices, showed an enhancement of PGE in the case of lipids. However, the contribution of aggregation in the observed PA properties at high BY-aniline concentrations remains an open question. To investigate this issue, it would be useful to synthetize a similar molecular agent with non-aggregative properties to reach the same BY-aniline high concentrations in SLNs, but without generating aggregates. A comparative study of the nanostructural, optical, and PA properties between the

two SLN types would likely isolate the structural effect of the matrix on PGE from the aggregation effect. Such a dye is currently under study, and experiments in this regard are being conducted in our consortium.

D. Material and methods

D.1. Materials.

Dexamethasone palmitate (DXP) was purchased from Interchim (France). 1,2-Distearoyl-sn-glycero-3-phosphoethanolamine-N-[methoxy(poly(ethylene glycol))-2000 (ammonium salt)] (DSPE-PEG$_{2000}$) was obtained from Avanti Polar Lipids, Inc. (USA) Palmitoyl chloride was purchased from Sigma-Aldrich. Milli-Q water was purified using a RIOS system from Merck-Millipore (France). All experiments except BODIPY-aniline-palmitate synthesis were performed in amber vials due to the photosensitivity of dexamethasone palmitate.

D.2. Synthesis of BODIPY-aniline-palmitate.

D.2.1) Materials

BODIPY-aniline-alcohol was prepared as described in Bodin et al.[12]. All other chemicals were received from commercial sources and used without further purification.

D.2.2) Instrumentations.

Solvent for synthesis (Carlo Erba) was purified with a MB SPS80 from MBraun. Flash chromatography was done on a Revelris X2 from Büchi. ^1H and ^{13}C NMR spectra were measured with a 400 MHz JEOL ECS. The residual signals from CDCl$_3$ (1H: δ 7.26 ppm; 13C: δ 77.00 ppm) were used as internal standards. The High-Resolution Mass Spectrometry data (HRMS) were obtained by direct infusion into ESI source using an Orbitrap Velos Pro hybrid mass spectrometer (Thermo Fisher Scientific) in positive ion mode. Fragmentation of standards was studied in FTMS by direct infusion in ESI source and product was dissolved in CHCl$_3$+MeOH.

D.2.3) Synthesis of BODIPY-aniline-palmitate (BY-aniline-Palm)

To an ice-cold and Argon degassed solution of BODIPY-aniline-alcohol (300 mg, 0.38 mmol), trimethylamine (80 μL, 0.61 mmol) and palmitoyl chloride (100 mg, 0.38 mmol) in dry dichloromethane (10 mL) DMAP (0.3 mg, 2.6 μmol) was added. The reaction mixture was warmed to room temperature and stirred overnight under inert atmosphere. The solvent was removed under reduced pressure and the crude product purified by flash chromatography (SiO$_2$, Petroleum ether: Dichloromethane, 0 to 80 v/v). The product was isolated in 77 % yield as a dark glassy solid. The reaction scheme is given in Fig. S1.

^1H NMR (400MHz, CDCl$_3$): δ 7.63 (d, 2H, J=14.5Hz, $\underline{H}$C=CH), 7.55 (d, 4H, J=8.7Hz, H$_{Ar}$), 7.26 (d, 2H, J=14.2Hz, $\underline{H}$C=CH), 6.74 (d, 4H, J=8.2Hz, H$_{Ar}$), 4.22 (t, 2H, J=6.4Hz, C$\underline{H_2}$-O), 3.25 (t, 2H, J=6.4Hz, C$\underline{H_2}$-S), 3.04 (s, 9H, NC$\underline{H_3}$), 2.65 (q, 4H, J=6.4Hz, C$\underline{H_2}$-CH$_3$), 2.32 (t, 2H, J=7.6Hz, C=OC$\underline{H_2}$),1.64 (m, 2H, C$\underline{H_2}$), 1.55 (s, 6H, C$\underline{H_3}$),
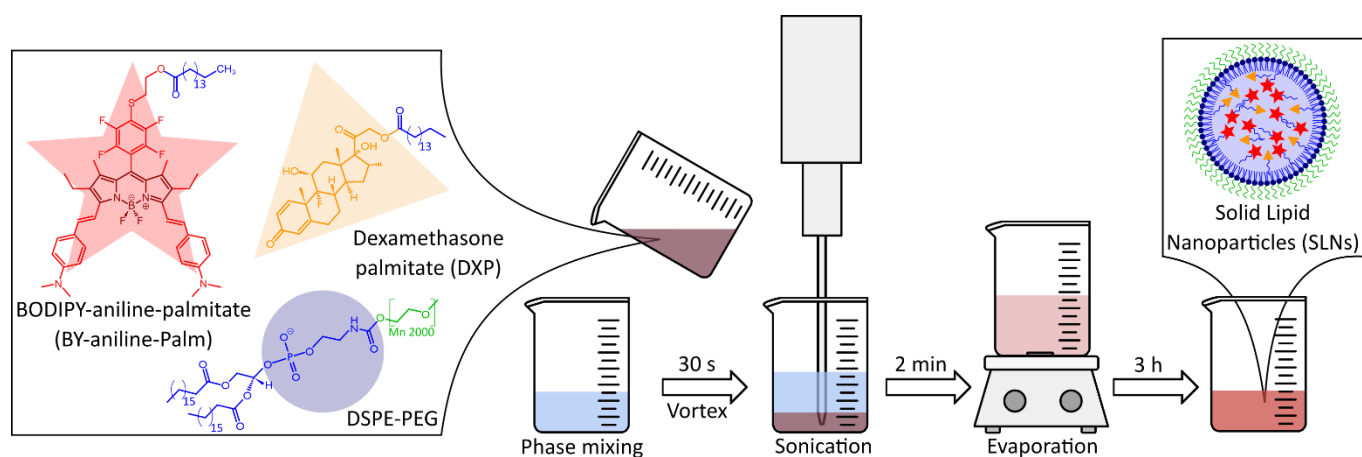
Fig. 5 – Scheme of the solid lipid nanoparticle (SLN) formulation process. All lipids are dissolved in chloroform (shown here with their schematic representations) and poured into water after a 30-s vortex, a 2-min evaporation and a 3-h evaporation, the SLNs (supposed structure shown in schematic representation: red star for BODIPY-aniline, yellow triangle for dexamethasone, blue circle for phosphatidylcholine head of DSPE-PEG, blue line for lipidic chain and green line for PEG chain) are available.

1.23-1.37 (m, 24H, C$\underline{H_2}$), 1.19 (t, 6H, J=7.5Hz, C$\underline{H_3}$-CH$_2$), 0.88 (t, 3H, J=6.9Hz, C$\underline{H_3}$) ppm.

^{13}C NMR (100MHz, CDCl$_3$): δ 173.5, 151.8, 151.1, 137.3, 129.2, 125.9, 115.8, 112.3, 62.0, 40.4, 34.2, 33.2, 32.1, 29.8, 29.7, 29.6, 29.5, 29.4, 29.3, 25.0, 22.8, 18.7, 14.3, 14.2, 10.7 ppm.

^{19}F RMN (CDCl$_3$, 376MHz): δ -132.3 (m, 2F), -138.6 (m, 2F), -139.3 (q, J$_{F-B}$=30.7 Hz, 2F) ppm

^{11}B RMN (CDCl$_3$, 128MHZ): δ 0.1 (t, J$_{B-F}$= 34.3 Hz) ppm

HRMS (ESI): *m/z*: calculated for [C$_{59}$H$_{75}$BF$_6$N$_4$O$_2$S] 1028.5608, found 1028.5592 [M+].

D.3. Nanoparticle Formulation.

Nanoparticles were formulated in two batches by an emulsion-evaporation process[2], from BY-aniline-Palm (1029 g.mol^{-1}), DXP (631 g.mol^{-1}) and DSPE-PEG$_{2000}$ (2806 g.mol^{-1}). 5 mL of Milli-Q water was prechilled at 4 °C and stock solutions of DXP and BY-aniline-Palm were prepared in chloroform.

The first batch, named Batch #1, was designed to obtain nine targeted final concentrations of BY-aniline-Palm with the following BY-aniline-Palm/DXP/DSPE-PEG$_{2000}$ mass ratios: 0.00/25.00/12.50; 0.41/24.59/12.50; 0.81/24.19/12.50; 2.36/22.64/12.50; 4.55/20.45/12.50; 8.81/16.19/12.50; 15.50/9.50/12.50; 20.76/4.24/12.50; and 25.00/0.00/12.50 in mg/5mL. This corresponds to a constant mass of DSPE-PEG$_{2000}$ (12.50 mg/5mL) for a molar ratio of BY-aniline-Palm/DXP of 0/100; 1/99; 2/98; 6/94; 12/88; 25/75; 50/50; 75/25 and 100/0. DXP solution was prepared at 20.0 mg/mL (2.53.10^{-2} mmol/mL) and BY-aniline-Palm one at 15.2 mg/mL (1.48.10^{-2} mmol/mL).

The second batch, named Batch #2, was designed to obtain five targeted final concentrations of BY-aniline-Palm (among the nine concentrations of Batch #1) with the following BY-aniline-Palm/DXP/DSPE-PEG$_{2000}$ mass ratios: 0.00/25.00/12.50; 0.81/24.19/12.50; 8.81/16.19/12.50; 15.50/9.50/12.50; and 25.00/0.00/12.50 in mg/5mL. This corresponds to a constant mass of DSPE-PEG$_{2000}$ (12.50 mg/5mL) for a molar ratio of BY-aniline-Palm/DXP of 0/100; 2/98; 25/75; 50/50 and 100/0.

For each formulation, the proper volume of each solution was taken through precision Hamilton syringes and the mixture was completed with chloroform to reach 2 mL. 12.5 mg of DSPE-PEG$_{2000}$ were added, and the organic phase was poured into the

5 mL water phase. The mixture was then pre-emulsified by vortexing for 30 s before being placed under ultrasonication in an ice bath during 2 min at an amplitude of 40% with Digital Sonifier 450 (Branson, USA) for batch #1 and Sonifier SFX150 for batch #2 (Branson, USA). The organic-phase evaporation was notably performed under room atmosphere of chemical hood for 3 hours with a 300-rpm stirring to ensure homogeneous soft evaporation conditions. After full evaporation of the solvent, the suspension volume was completed to 5 mL with Milli-Q water in a volumetric flask, and nanoparticles were stored at 4 °C protected from light.

The SLN-2% formulation corresponds to a BY-aniline-Palm molar concentration of 1.56×10^{-1} mmol/L which is comparable to the BY-aniline-PLA-50% formulation (BY-aniline-PLA molar concentration of 1.67×10^{-1} mmol/L) in reference[12]. We reproduced the formulation protocol of [12] to get a BY-aniline-PLA-47% formulation (corresponding to a BY-ani-PLA molar concentration of 1.56×10^{-1} mmol/L). Briefly, 11.75 mg of BY-ani-PLA and 13.25 mg of DSPE-PEG$_{5000}$ were put in 2 mL of chloroform and poured into 5 mL of a cold solution of sodium cholate (15 g/L). After 30 s of vortexing and ultrasonication in an ice bath during 1 min at an amplitude of 30% with Sonifier SFX150 (Branson, USA), organic phase was evaporated under chemical hood for 3 hours with a 300-rpm stirring. Sodium cholate was removed by ultracentrifugation for 1h at 4°C and 40000 rpm (Optima LE-80K Ultracentrifuge Beckman Coulter, USA). The obtained solid was resuspended in milli-Q water to a final polymer concentration of 5 mg/mL.

D.4. Size and ζ Potential Measurement.

Size and ζ potential were determined with a Zetasizer Nano-ZS from Malvern Instrument (UK), based on quasi-elastic light scattering. The measurement was performed with 633 nm laser in triplicate at a backscattered angle of 173° at 25°C but also, when mentioned for the size measurement, at 15°C and 35°C. Hydrodynamic diameter (d$_H$) and polydispersity index (PdI) were recorded on 1/20 diluted samples in Milli-Q water, and ζ potential measurements on 1/10 diluted samples in NaCl 1 mM.

D.5. Nanoparticle tracking analysis (NTA).

Nanoparticle tracking analysis (NTA) using the NanoSight LM10 instrument (NanoSight, Amesbury, UK) was carried out to assess the number of nanoparticles per mL after a 10000-fold or 20000-fold dilution in water. The signal was collected using a sCMOS camera and a 405 nm monochromatic laser. For all the experiments, the following parameters were defined in the acquisition software: a controlled temperature of 25.0°C a camera level of 13 and a detection threshold of 5. Measurements were done in quintuplicate; mean value and standard deviation are indicated. By divided the BY-aniline-PLA or -Palm concentration in the formulation by the number of particles, we obtain the number of BY-aniline by particle.

D.6. Transmission Electron Microscopy (TEM).

Transmission electron microscopy was performed at I2BC (CNRS, Gif-sur-Yvette, France). A volume of 5 µL of the nanoparticle suspension at 3.5 mg/mL lipid was deposited for 1 min on glow-discharged 400 mesh formvar-coated copper grids. Negative staining was performed by addition of a drop of uranyl acetate at 2% w/w for 15 s repeated twice. Excess solution was removed, and grids were left to dry before observation. The observations were carried out on a JEOL JEM-1400 microscope (Japan) at an acceleration voltage of 120 kV. Images were acquired using an Orius camera (Gatan Inc., USA).

D.7. Photophysical Measurements
D.7.1) UV-visible solution spectra

Measurements were carried out in 10 mm pathlength quartz cuvettes. Absorption spectra were recorded using a UV–visible spectrophotometer UV-2600 (Shimadzu, Japan) with an integrating sphere coated with barium sulphate ISR-2600PLUS to minimize scattering signal. Transmission measurements were performed with a direct acquisition of the absorbance signal.

Scattering was suppressed by the use of the integration sphere and by the use of unloaded particles as spectral blank (Fig. S5). Spectra were measured at constant concentration of BY-aniline-Palm ($1.73.10^{-2}$ mM) corresponding to an optical density around 1. The dilutions in Milli-Q water required are given in Table S1 and the spectra are then corrected from the real BY-aniline-Palm concentration to the targeted one.

For the second batch, supplementary absorption spectra were recorded using a spectrophotometer V-650 (Jasco, Japan) with a Peltier system to precisely control on the acquisition temperature. Spectra were recorded at 15 °C, 25 °C and 35 °C consistently with photoacoustic spectra measurements.

D.7.2) UV-visible solid-state spectra

A small quantity of BODIPY-aniline was dissolved in toluene. A drop of each solution was placed on microscope slides and then spread with a small slide to form a homogeneous film during evaporation, The UV–visible spectrum was recorded with the set-up described above.

D.7.3) Fluorescence spectra

Fluorescence emission spectra were recorded using a Fluoromax-4 spectrofluorometer (Jobin-Yvon, Horiba, Japan), for Batch #1 and a Fluorolog-3 spectrofluorometer (Jobin-Yvon, Horiba, Japan) with double system of detection (UV-visible and IR range) for Batch #2. Intensity signals corrected from the lamp fluctuations, and the instrument response function were recorded with emitter and detector slits width of 10 nm. Solutions were diluted to avoid inner filter effects: absorbance below 0.1 over the whole wavelength range. Fluorescence signals were normalized to account for the absorbance (A_{730}) at the excitation wavelength (730 nm): $I_{corr} = \frac{I}{1-10^{-A_{730}}}$.

D.7.4) Transient absorption spectroscopy

Transient absorption spectroscopy experiments were performed with a home-built setup[38]. Briefly, a Nd-YAG laser (EKSPLA, 4 ns, 10 Hz, 8 mW) with an optical parametric oscillator was used as a pump at 680 nm. A ns pulse white light continuum laser (LEUKOS, 20Hz) was used as a probe. The probe beam was separated into two different pathways, one used as a reference to correct the pulse-to-pulse energy fluctuation (detection with a Princeton Instrument CCD (ICCD) detector PIMAX 4) and the other to probe the sample. The probing arm after passing the sample is coupled into a round to linear optical fibre bundle before being analysed by a spectrograph SPEX 270M (Jobin-Yvon). Detection of the dispersed white light is performed by an intensified CCD (ICCD) detector PIMAX 4 (Princeton Instrument). The measured differential absorbance is defined as: $\Delta A(\lambda, t) = -\log \frac{I_{probe}^{on}}{I_{ref}^{on}} + \log \frac{I_{probe}^{off}}{I_{ref}^{off}}$ with I_{probe}^{on} and I_{ref}^{on} the probe and reference signal when the pump laser is on, and I_{probe}^{off} and I_{ref}^{off} the probe and reference signal when the pump is off. Spectra were obtained in 10 mm path length quartz cuvettes with a volume of 1 mL. For all samples, absorbance spectra were checked before and after the measure to ensure that the samples had not been degraded by the pump laser (which was never the case).

D.8. Photoacoustic Spectra Measurements.
D.8.1) Photoacoustic Spectroscopy

Photoacoustic (PA) spectra of SLN suspensions were measured with a calibrated PA spectrometer described in detail in Lucas et al.[13]. Briefly, optical excitation was generated with a tunable (680−980 nm) nanosecond Laser (pulse repetition rate: 20 Hz, pulse width 6 - 7 ns, SpitLight 600OPO, Innolas, Germany). The optical wavelength was scanned from 680 nm to 970 nm in 10 nm steps. To limit potential photodegradation, the per-pulse tunability of the laser was used and successive laser pulses had a different optical wavelength. A total of 15 wavelength scans (sweeps) were carried out (450 successive laser pulses). Ultrasound (US) detection was performed with a linear US array (L7−4, ATL, USA) driven by a programmable US machine (Vantage, Verasonics, USA). Samples were injected in 4 PTFE tubes (inner diameter: 0.2 mm, wall thickness: 0.1 mm, Bola, Germany) with a 50-µL glass syringe (Hamilton). Excitation light on the sample had a maximum fluence of 4.5 mJ·cm⁻², and 1.5 cm of the tube was illuminated. The tube and the US detector were immersed in a thermostatic water tank (T100-ST12 Optima, Grant, UK) maintained at 15 °C, 25 °C or 35 °C. The water bath temperature was monitored during the whole experiment (HI98509, Hanna instruments, Lingolsheim, France). The PA spectrometer was calibrated with two reference
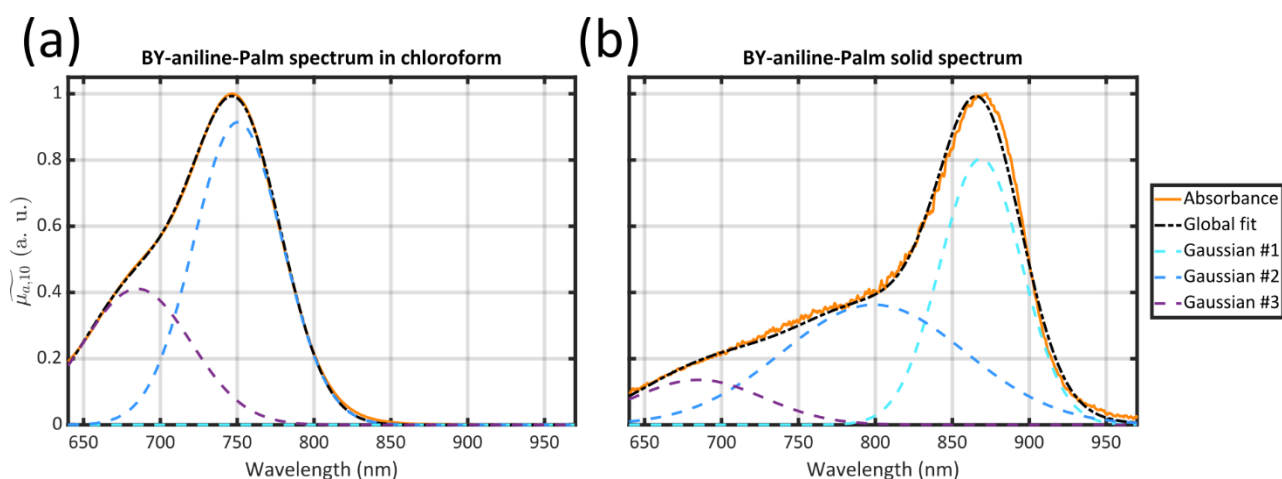
Fig. 6 – Decomposition in the sum of three Gaussian functions of the absorption spectrum of BODIPY-aniline-Palm (a) in chloroform and (b) in solid state after drop casting. From left to right, the Gaussian functions are centred at 685 nm (purple), 750-799 nm (blue) and 860-869 nm (cyan).

solutions, following the process described in ref[20]. The first one is a solution of CuSO$_4$·5H$_2$O (ACS reagent, ≥98.0%, Sigma-Aldrich, St. Louis, MO, USA) at a concentration of 0.25 M (or 62.4 g.L^{-1}) and allowed the per-wavelength calibration thanks to its strong absorption all over the considered NIR wavelength. The second one is a solution of nigrosin (Nigrosin, 198285, Sigma-Aldrich, St. Louis, MO, USA) at a concentration of 173 mg.L^{-1} and allowed the amplitude calibration thanks to its Grüneisen coefficient equal to the one of water. Following this calibration, samples were injected successively in the same 4 tubes. We verified that no detectable absorption remained in the tubes between two samples by systematically measuring a background reference (water). This background reference was also used as a blank for PA measurements. No noticeable change in the measured spectra was observed over the 15 wavelength scans, and the iterations were then averaged to increase the signal-to-noise ratio. The PA spectra were computed and converted in spectroscopic units to obtain the decadic photoacoustic coefficient: θ_{10}^{PA}.

The samples were injected twice in the four tubes for a total of 8 measurements per sample. The median value and the median absolute deviation with a scaling factor 1.4826 were computed over the 8 measurements to obtain the photoacoustic coefficient and its deviation. In this paper, we call MAD the median absolute deviation with a scaling factor 1.4826.

Gold nanoparticles were also used as external reference compound. Au@DTDTPA 8-nm particles, synthesized at Université de Franche-Comté (CNRS, Institut UTINAM, Besançon, France)[20] were selected because of their PGE equal to 1 over the entire wavelength range according to Lucas et al.[20].

D.8.2) Photoacoustic Quantification

The Photoacoustic Generation Efficiency (PGE) was defined in eq. 2 as the product of the photothermal conversion efficiency (PTCE) and the effective Grüneisen coefficient of the solution relative to water. It is also defined as the ratio between the

decadic photoacoustic coefficient and the decadic absorption coefficient.

$$PGE(\lambda) = \frac{\theta_{10}^{PA}(\lambda)}{\mu_{a,10}(\lambda)} \qquad (3)$$

We also define the Global Photoacoustic Efficiency (GPAE) as it was defined by Bodin *et al.*[15]. GPAE is the ratio between the integral of the PA spectrum and the integral of the corresponding absorption spectrum on the interval $[\lambda_1 = 680 \text{ nm}, \lambda_2 = 920 \text{ nm}]$. It can be seen as the weighted mean PGE over the whole spectrum.

$$GPAE = \frac{\int_{\lambda_1}^{\lambda_2} \theta_{10}^{PA}(\lambda) \, d\lambda}{\int_{\lambda_1}^{\lambda_2} \mu_{a,10}(\lambda) \, d\lambda} \qquad (4)$$

The integrals were calculated on the experimental data with the trapezoidal rule.

D.9. Spectra decomposition

We implemented a decomposition of the absorption spectra and the PA spectra into the sum of three Gaussian functions. We used a fitting algorithm based on a nonlinear least-squares solver (trust-region-reflective method) to determine the amplitude a_i (cm^{-1}), the central wavelength λ_i (nm) and the Gaussian Root Mean Square (RMS) width ω_i (nm) of each Gaussian function of the sum: $S(\lambda) = \sum_i a_i \cdot \exp\left(-\frac{(\lambda - \lambda_i)^2}{2\omega_i^2}\right)$ with $i \in [\![1,3]\!]$. ω_i is proportional to the full width half maximum (FWHM) of the Gaussian function ($FWHM_i = 2\sqrt{2 \ln 2} \cdot \omega_i$).

Absorption spectra between 640 nm and 980 nm were decomposed into the sum of 3 Gaussian functions. The Gaussian functions were numbered by decreasing central wavelength: $\lambda_1 \approx 865 \, nm$, $\lambda_2 \approx 780 \, nm$ and $\lambda_3 = 685 \, nm$. An illustration of this decomposition is given in Fig. 6 for the absorption spectra of BY-aniline-Palm in solution (Gaussian #2 and #3) and in solid-state (Gaussian #1 to #3). PA spectra between 680 nm and 930 nm were modelled for the SLN suspensions by the sum of 3 Gaussian curves with the same central wavelengths λ_1, λ_2 and λ_3. For each SLN batch, the

parameter determination was achieved by simultaneous and joint optimization of the curve fitting for both the absorption spectrum and the PA spectrum.

In the following, parameters for the PA spectrum are identified with a prime symbol, while the parameters for the absorption spectrum have no prime symbol. To help the algorithm convergence, central wavelengths for Gaussian functions #1 and #2 were set equal with a ± 5 nm tolerance between the absorption spectrum and the PA spectrum, especially because the absorption spectrum has a 0.5 nm step while the PA spectrum has a 10 nm step. Therefore, a first constrain was $\lambda_i' = \lambda_i \pm 5$ nm for $i < 3$. The RMS widths were set equal: $\omega_i' = \omega_i$. Amplitudes a_i' and a_i were not coupled. Additional constrains were applied for the different bands but remain the same for all SLN batches. For Gaussian function #3, the central wavelength was set equal to $\lambda_3 = \lambda_3' = 685$ nm, because of the vicinity between the central wavelength and the lower wavelength limit of the PA spectrum. For Gaussian function #2, the central wavelength and the RMS width were bounded by the results of solid-state spectrum decomposition i.e. $\lambda_2 < 799$ nm and $\omega_2 < 59.5$ nm. Finally, for Gaussian function #1, we determined that the amplitude a_1 has non-significant values for BY-aniline-Palm percentage below 50% and it was set equal to $a_1 = 0$. The RMS width was set equal to the RMS width found in the solid-state spectrum decomposition i.e. $\omega_1 = 26.5$ nm.

The areas of the Gaussian functions were calculated with the analytic expression of the adimensional integral:

$$A_i = \int_{-\infty}^{\infty} a_i \cdot \exp\left(-\frac{(\lambda - \lambda_i)^2}{2\omega_i^2}\right) d\lambda = a_i \cdot \omega_i \cdot \sqrt{2\pi} \cdot 10^{-7} \quad (5)$$

We then use the Band Photoacoustic Efficiency (BPAE) defined in ref[15] as the ratio of the PA band area by the corresponding absorption band area. In our case, as the RMS widths of the Gaussian functions were set equal for the PA and absorption decompositions, the BPAE can be computed by a ratio of amplitudes (Table S3).

$$BPAE_i = \frac{A_i^{PA}}{A_i^{Abs}} = \frac{a_i^{PA}}{a_i^{Abs}} \quad (6)$$

Conclusions

We have successfully labelled SLNs with a BODIPY-aniline for PAI, using a simple and direct one-pot formulation protocol. Our particle design enabled to study the absorption and PA spectral transformations as a function of the percentage of dyes incorporated in the SLN. Highly absorbing SLNs with remarkable absorption cross section per mole of particles were obtained. Despite significant spectral modifications, modelling the spectrum as a sum of three Gaussian functions allowed us to simplify the study to the interplay of three spectral bands, which were attributed to different photophysical phenomena (vibration, absorption, and aggregation). The interplay was quantitatively demonstrated. A precise measurement of the PA generation efficiency over the entire spectrum, per band, and

per wavelength highlighted the enhancement of the PA signal caused by the lipid core (PGE above 1), in comparison to previously described polymer particles, and raised questions about the involvement of different energy conversions (light to heat and thermodynamic expansion) in the per-band variations of the efficiency. Additional PA experiments were conducted by varying the ambient temperature and the excitation fluence to clarify these points. This study clearly opens the way to careful consideration of the optical and photothermal phenomena at stake in optically labelled nanoparticles for photoacoustic imaging, in particular when building materials, such as lipids, possess a Grüneisen coefficient larger than water.

Author Contributions

J. G., N. T., C. L., R. M. and G. C. are responsible for the conceptualization of the project and experiments. C. L., N. T. and J.G. developed the SLN formulation. C. L. and G. M. performed the SLN formulations. C. L. and G. M. performed the photoacoustic and spectrophotometric measurements. C. L., J. G., N. T. and R. M. analysed and evaluated the data. G. C. developed, prepared and characterized the BY-aniline. G. C. and C. L. synthetized and characterized the BY-aniline-Palm. All authors discussed and contributed to the preparation of the manuscript.

Conflicts of interest

There are no conflicts to declare.

Data availability

The data supporting this article have been included as part of the Electronic Supplementary Information.

Notes and references

1   J. Akbari, M. Saeedi, F. Ahmadi, S. M. H. Hashemi, A. Babaei, S. Yaddollahi, S. S. Rostamkalaei, K. Asare-Addo and A. Nokhodchi, *Pharm. Dev. Technol.*, 2022, **27**, 525–544.

2   M. Lorscheider, N. Tsapis, R. Simón-Vázquez, N. Guiblin, N. Ghermani, F. Reynaud, R. Canioni, S. Abreu, P. Chaminade and E. Fattal, *Mol. Pharm.*, 2019, **16**, 2999–3010.

3   M. Lorscheider, N. Tsapis, M. ur-Rehman, F. Gaudin, I. Stolfa, S. Abreu, S. Mura, P. Chaminade, M. Espeli and E. Fattal, *J. Control. Release*, 2019, **296**, 179–189.

4   K. Oumzil, M. A. Ramin, C. Lorenzato, A. Hémadou, J. Laroche, M. J. Jacobin-Valat, S. Mornet, C.-E. Roy, T. Kauss, K. Gaudin, G. Clofent-Sanchez and P. Barthélémy, *Bioconjug. Chem.*, 2016, **27**, 569–575.

5   E. Andreozzi, P. Wang, A. Valenzuela, C. Tu, F. Gorin, M. Dhenain and A. Louie, *Bioconjug. Chem.*, 2013, **24**, 1455–1467.

6   G. Chinigò, A. Gonzalez-Paredes, A. Gilardino, N. Barbero, C. Barolo, P. Gasco, A. Fiorio Pla and S. Visentin, *Spectrochim. Acta A Mol. Biomol. Spectrosc.*, 2022, **271**, 120909.

7   V. Ntziachristos, *Nat. Methods*, 2010, **7**, 603–614.

8   P. C. Beard, *Interface Focus*, 2011, **1**, 602–631.

9   J. Weber, P. C. Beard and S. E. Bohndiek, *Nat. Methods*, 2016, **13**, 639–650.

10 R. E. Borg and J. Rochford, *Photochem. Photobiol.*, 2018, **94**, 1175–1209.

11 P. Ramezani, S. C. De Smedt and F. Sauvage, *Bioengineering & Transla Med*, 2024, e10652.

12 J.-B. Bodin, J. Gateau, J. Coïs, T. Lucas, F. Lefebvre, L. Moine, M. Noiray, C. Cailleau, S. Denis, G. Clavier, N. Tsapis and R. Méallet-Renault, *ACS Appl. Mater. Interfaces*, 2022, 40501–40512.

13 T. Lucas, M. Sarkar, Y. Atlas, C. Linger, G. Renault, F. Gazeau and J. Gateau, *Sensors*, 2022, **22**, 6543.

14 Q. Fu, R. Zhu, J. Song, H. Yang and X. Chen, *Adv. Mater.*, 2019, **31**, 1805875.

15 J.-B. Bodin, C. Linger, J. Gateau, T. Beguin, T. Lucas, L. Moine, D. Chapron, M.-H. Ha-Thi, A. Fatima, G. Clavier, N. Tsapis and R. Méallet, *J. Phys. Chem. C*, 2023, **127**, 18971–18985.

16 W. Hu, X. Miao, H. Tao, A. Baev, C. Ren, Q. Fan, T. He, W. Huang and P. N. Prasad, *ACS Nano*, 2019, **13**, 12006–12014.

17 S. Choi, J. Bouffard and Y. Kim, *Chem. Sci.*, 2014, **5**, 751–755.

18 K. Li, X. Duan, Z. Jiang, D. Ding, Y. Chen, G.-Q. Zhang and Z. Liu, *Nat. Commun.*, 2021, **12**, 2376.

19 J. L. Bricks, Y. L. Slominskii, I. D. Panas and A. P. Demchenko, *Methods Appl. Fluoresc.*, 2017, **6**, 012001.

20 T. Lucas, C. Linger, T. Naillon, M. Hashemkhani, L. Abiven, B. Viana, C. Chaneac, G. Laurent, R. Bazzi, S. Roux, S. Becharef, G. Avveduto, F. Gazeau and J. Gateau, *Nanoscale*, 2023, **15**, 17085–17096.

21 T. Stahl, T. Allen and P. Beard, eds. A. A. Oraevsky and L. V. Wang, San Francisco, California, United States, 2014, p. 89435H.

22 J. P. Fuenzalida Werner, Y. Huang, K. Mishra, R. Janowski, P. Vetschera, C. Heichler, A. Chmyrov, C. Neufert, D. Niessing, V. Ntziachristos and A. C. Stiel, *Anal. Chem.*, 2020, **92**, 10717–10724.

23 T. Stahl, R. Bofinger, I. Lam, K. J. Fallon, P. Johnson, O. Ogunlade, V. Vassileva, R. B. Pedley, P. C. Beard, H. C. Hailes, H. Bronstein and A. B. Tabor, *Bioconjugate Chem.*, 2017, **28**, 1734–1740.

24 S. Liang, B. Lashkari, S. S. S. Choi, V. Ntziachristos and A. Mandelis, *Photoacoustics*, 2018, **11**, 56–64.

25 M. Duquesne, C. Mailhé, S. Doppiu, J.-L. Dauvergne, S. Santos-Moreno, A. Godin, G. Fleury, F. Rouault and E. Palomo Del Barrio, *Materials*, 2021, **14**, 4707.

26 O. Zmeskal, L. Marackova, T. Lapcikova, P. Mencik and R. Prikryl, Smolenice, Slovakia, 2020, p. 020022.

27 V. K. Pustovalov, *Nanotechnology and Precision Engineering*, 2024, **7**, 015001.

28 M. Pyda, R. C. Bopp and B. Wunderlich, *J. Chem. Thermodyn.*, 2004, **36**, 731–742.

29 H. Aoki, M. Nojiri, R. Mukai and S. Ito, *Nanoscale*, 2014, **7**, 337–343.

30 G. A. Pang, F. Poisson, J. Laufer, C. Haisch and E. Bossy, *J. Phys. Chem. C*, 2020, **124**, 1088–1098.

31 O. Simandoux, A. Prost, J. Gateau and E. Bossy, *Photoacoustics*, 2015, **3**, 20–25.

32 A. Prost, F. Poisson and E. Bossy, *Phys. Rev. B*, 2015, **92**, 115450.

33 A. Kumari, K. Kumari and S. Gupta, *Sci. Rep.*, 2019, **9**, 20334.

34 S. Jaiswal, S. B. Dutta, D. Nayak and S. Gupta, *ACS Omega*, 2021, **6**, 34842–34849.

35 G. Marbán, T. T. Vu and T. Valdés-Solís, *Appl. Catal. A-Gen*, 2011, **402**, 218–223.

36 D. K. Das, K. Makhal, S. N. Bandyopadhyay and D. Goswami, *Sci Rep*, 2014, **4**, 6097.

37 K. Zlatić, H. B. E. Ayouchia, H. Anane, B. Mihaljević, N. Basarić and T. Rohand, *J. Photochem. Photobiol. A, Chem*, 2020, **388**, 112206.

38 A. Fatima, J. Rabah, E. Allard, H. Fensterbank, K. Wright, G. Burdzinski, G. Clavier, M. Sliwa, T. Pino, R. Méallet-Renault, K. Steenkeste and M.-H. Ha-Thi, *Photochem Photobiol Sci*, 2022, **21**, 1573–1584.

39 C. Gómez-Gaete, N. Tsapis, L. Silva, C. Bourgaux, M. Besnard, A. Bochot and E. Fattal, *Eur. J. Pharm. Biopharm.*, 2008, **70**, 116–126.

40 C. C. L. Cheung, G. Ma, K. Karatasos, J. Seitsonen, J. Ruokolainen, C.-R. Koffi, H. A. F. M. Hassan and W. T. Al-Jamal, *Nanotheranostics*, 2020, **4**, 91–106.

41 D. Miranda, H. Huang, H. Kang, Y. Zhan, D. Wang, Y. Zhou, J. Geng, H. I. Kilian, W. Stiles, A. Razi, J. Ortega, J. Xia, H. S. Choi and J. F. Lovell, *Theranostics*, 2019, **9**, 381–390.

42 B. Changalvaie, S. Han, E. Moaseri, F. Scaletti, L. Truong, R. Caplan, A. Cao, R. Bouchard, T. M. Truskett, K. V. Sokolov and K. P. Johnston, *ACS Appl. Mater. Interfaces*, 2019, **11**, 46437–46450.

43 M. R. Kawelah, S. Han, C. Atila Dincer, J. Jeon, J. Brisola, A. F. Hussain, A. S. Jeevarathinam, R. Bouchard, A. E. Marras, T. M. Truskett, K. V. Sokolov and K. P. Johnston, *ACS Appl. Mater. Interfaces*, 2024, **16**, 5598–5612.

44 C. A. Wood, S. Han, C. S. Kim, Y. Wen, D. R. T. Sampaio, J. T. Harris, K. A. Homan, J. L. Swain, S. Y. Emelianov, A. K. Sood, J. R. Cook, K. V. Sokolov and R. R. Bouchard, *Nat. Commun.*, 2021, **12**, 5410.

45 W. Xu, J. Leskinen, T. Sahlström, E. Happonen, T. Tarvainen and V.-P. Lehto, *Photoacoustics*, 2023, **33**, 100552.